

**PHOTOCATALYTIC DEGRADATION OF
RHODAMINE B IN GREYWATER OVER
ZnO/BiOBr/MgFe₂O₄ TERNARY
NANOCOMPOSITE UNDER SUNLIGHT
IRRADIATION: PERFORMANCE
EVALUATION, KINETIC AND
PHYTOTOXICITY STUDIES**

LIM KHAR LOK

UNIVERSITI TUNKU ABDUL RAHMAN

**PHOTOCATALYTIC DEGRADATION OF RHODAMINE B IN
GREYWATER OVER ZnO/BiOBr/MgFe₂O₄ TERNARY NANOCOMPOSITE
UNDER SUNLIGHT IRRADIATION: PERFORMANCE EVALUATION,
KINETIC AND PHYTOTOXICITY STUDIES**

LIM KHAR LOK

**A project report submitted in partial fulfilment of the requirements for the
award of Bachelor of Engineering (HONS) Petrochemical Engineering**


Faculty of Engineering and Green Technology

Universiti Tunku Abdul Rahman

May 2022

DECLARATION


I hereby declare that this project report is based on my original work except for citations and quotations which have been duly acknowledged. I also declare that it has not been previously and concurrently submitted for any other degree or award at UTAR or other institutions.

Signature : 
Name : LIM KHAR LOK
ID. No. : 1702889
Date : 23 APRIL 2022

APPROVAL FOR SUBMISSION


I certify that the project report entitled “**PHOTOCATALYTIC DEGRADATION OF RHODAMINE B IN GREYWATER OVER ZnO/BiOBr/MgFe₂O₄ TERNARY NANOCOMPOSITE UNDER SUNLIGHT IRRADIATION: PERFORMANCE EVALUATION, KINETIC AND PHYTOTOXICITY STUDIES**” was prepared by **LIM KHAR LOK** has met the required standard for submission in partial fulfilment of the requirements for the award of Bachelor of Engineering (Hons) Petrochemical Engineering at Universiti Tunku Abdul Rahman.

Approved by,

Signature : 

Supervisor : ChM. Ts. Dr. Sin Jin Chung

Date : 23 APRIL 2022

Signature : 

Co-supervisor : ChM. Ts. Dr. Lam Sze Mun

Date : 23 APRIL 2022

The copyright of this report belongs to the author under the terms of the copyright Act 1987 as qualified by Intellectual Property Policy of Universiti Tunku Abdul Rahman. Due acknowledgement shall always be made of the use of any material contained in, or derived from, this report.

© 2022, Lim Khar Lok. All right reserved.

ACKNOWLEDGEMENTS

I would like to express my deepest and sincere gratitude to my supervisor, ChM. Ts. Dr. Sin Jin Chung for his endless patience, noble guidance, immense knowledge, enthusiasm and support with full encouragement. My sincere thanks also go to my moderators, Dr. Ong Yit Thai and Dr. Toh Pey Yi for their insightful feedbacks.

Further, yet importantly, I wish to show my appreciation to all the helpful lab officers especially Mrs. Ropidah Hamimi binti Mohd Zain, Ms. Lim Cheng Yen and Mr. Yong Tzyy Jeng for their greatest assistance in providing technical support during the completion of Final Year Project.

Last, but not the least, my warm and heartfelt thanks go to my family members and friends for their unconditional, unequivocal and loving support all through my studies. I wish to extend my special thanks to my lab mates as well as seniors, Chin Ying Hui and Tan Jin Han for their continuous support and valuable advice during the course of this project.

**PHOTOCATALYTIC DEGRADATION OF RHODAMINE B IN
GREYWATER OVER ZnO/BiOBr/MgFe₂O₄ TERNARY
NANOCOMPOSITE UNDER SUNLIGHT IRRADIATION:
PERFORMANCE EVALUATION, KINETIC AND PHYTOTOXICITY
STUDIES**

ABSTRACT

Extensive use of dye in various industries, particularly textile industries, along with the leaching from household sources into greywater has led to environmental and human health hazard. Among the existing advanced oxidation processes (AOPs), semiconductor-mediated photocatalysis is intensively recognized as a potential and promising alternative for the treatment of dye effluent. In this study, a new, efficient and magnetically separable ZnO/BiOBr/MgFe₂O₄ nanocomposite was successfully fabricated via a facile ultrasonic-precipitation method. A series of analytical characterization methods were employed to examine the physicochemical and optical properties of prepared photocatalyst. FESEM showed the homogeneous adhesion of ZnO nanoparticles and MgFe₂O₄ nanorods on the two-dimensional BiOBr nanosheets, forming a ternary heterostructure. UV-vis DRS confirmed the elevated visible light photosensitivity and reduced band gap of prepared ZnO/BiOBr/MgFe₂O₄ nanocomposite. Photocatalytic performance of ZnO/BiOBr/MgFe₂O₄ was investigated by the degradation of RhB in both aqueous solution and greywater under solar light illumination. As compared to the single-phase component photocatalysts, the prepared ZnO/BiOBr/MgFe₂O₄ exhibited remarkably enhanced photocatalytic activity with RhB degradation efficiency up to 96.14% and 93.59% in aqueous solution and greywater, respectively, with corresponding apparent rate constant of 0.0153 min⁻¹ and 0.017 min⁻¹ after 180 min irradiation. The boosted photoactivity of nanocomposite was attributed to the synergistic effect among the ZnO, BiOBr and MgFe₂O₄ which significantly reduced the charge carrier recombination and improved the charge migration behaviour. The phytotoxicity study also revealed that the phytotoxicity of RhB has been substantially reduced after the photocatalytic degradation over the as-synthesized ternary composite. The present work paves the way for future development and

potential application of ZnO/BiOBr/MgFe₂O₄ in remediation of wastewater and household greywater.

TABLE OF CONTENTS

DECLARATION		ii
APPROVAL FOR SUBMISSION		iii
ACKNOWLEDGEMENTS		v
ABSTRACT		vi
TABLE OF CONTENTS		viii
LIST OF TABLES		xi
LIST OF FIGURES		xii
LIST OF SYMBOLS/ABBREVIATIONS		xiv
CHAPTER		
1	INTRODUCTION	1
	1.1 Background of Study	1
	1.2 Problem Statement	4
	1.3 Objectives	6
	1.4 Scope of Study	6
2	LITERATURE REVIEW	7
	2.1 Review of Dye in Wastewater	7
	2.2 Usage of Hazardous Effects of Rhodamine B	12
	2.3 Heterogeneous Photocatalysis	14
	2.4 ZnO as Photocatalyst	16
	2.5 Mechanism of ZnO Photocatalysis	21
	2.6 ZnO/BiOBr/MgFe ₂ O ₄ ternary Z-scheme nanocomposite	24
	2.7 Phytotoxicity	28

3	METHODOLOGY	30
3.1	Overall Flowchart of Work	30
3.2	Materials and Chemicals	31
3.3	Photocatalyst Fabrication	32
3.4	Characterization	35
3.4.1	X-ray Diffraction (XRD)	35
3.4.2	Field Emission Scanning Electron Microscopy (FESEM) and Energy Dispersive X-ray (EDX) Spectroscopy	35
3.4.3	Ultraviolet-Visible Diffuse Reflectance Spectroscopy (UV-vis DRS)	36
3.4.4	Fourier Transform Infrared Spectroscopy-Attenuated Total Reflectance (FTIR-ATR)	36
3.5	Photocatalytic Activity	37
3.6	Phytotoxicity Test	39
4	RESULTS AND DISCUSSION	40
4.1	Characterization	40
4.1.1	Field Emission Scanning Electron Microscopy (FESEM)	40
4.1.2	Energy Dispersive X-ray (EDX)	42
4.1.3	Fourier Transform Infrared Spectroscopy-Attenuated Total Reflectance (FTIR-ATR)	44
4.1.4	Ultraviolet-Visible Diffuse Reflectance Spectroscopy (UV-vis DRS)	46
4.1.5	X-Ray Diffraction (XRD)	49
4.2	Photocatalytic Degradation Studies	51
4.3	Phytotoxicity Evaluation	57
5	CONCLUSION AND RECOMMENDATION	59
5.1	Conclusion	59

5.2 Recommendation

60

REFERENCES

61

LIST OF TABLES

TABLE	TITLE	PAGE
2.1	Wastewater Discharge Standard	10
2.2	Physicochemical properties of Rhodamine B	12
2.3	Photocatalytic activity of ZnO on various pollutant	19-20
2.4	Photocatalytic activity of ZnO-based ternary nanocomposite on various pollutants	27
3.1	List of materials and chemicals used	31

LIST OF FIGURES

FIGURE	TITLE	PAGE
2.1	Contribution of textile industry to water pollution in different states of Malaysia.	8
2.2	Average water usage distribution (%) in Malaysia.	9
2.3	Schematic illustration of the key aspects governing the photo-efficiency of semiconductor.	15
2.4	Stick and ball representation of ZnO crystal structures: (a) cubic rocksalt, (b) cubic zinblende and (c) hexagonal wurtzite.	16
2.5	Degradation of organic pollutant by ZnO under solar irradiation.	23
3.1	Flowchart of Overall Experimental Study.	30
3.2	Illustration of ZnO preparation.	32
3.3	Synthesis of BiOBr nanoparticles.	33
3.4	Preparation route of MgFe ₂ O ₄ nanoparticles.	34
3.5	Synthesis process of ZnO/BiOBr/MgFe ₂ O ₄ nanocomposites.	35
3.6	Experimental Setup for Photodegradation of Rhodamine B in aqueous solution.	37
3.7	Calibration curve of absorbance against RhB concentration	38
4.1	FESEM images obtained for (a) ZnO; (b) BiOBr; (c) MgFe ₂ O ₄ and (d) ZnO/BiOBr/MgFe ₂ O ₄ .	41
4.2	(a) The EDX spectra of ZnO/BiOBr/MgFe ₂ O ₄ ; (b)-(h) elemental dot mapping of ZnO/BiOBr/MgFe ₂ O ₄ .	43
4.3	FTIR-ATR spectra of ZnO, BiOBr, MgFe ₂ O ₄ and ZnO/BiOBr/MgFe ₂ O ₄ .	45
4.4	UV-vis diffuse reflectance spectra of ZnO, BiOBr, MgFe ₂ O ₄ and ZnO/BiOBr/MgFe ₂ O ₄ .	47

4.5	Energy gap analysis of ZnO, BiOBr, MgFe ₂ O ₄ and ZnO/BiOBr/MgFe ₂ O ₄ via Tauc plot.	48
4.6	XRD spectra of as-obtained photocatalysts: (a) ZnO, (b) BiOBr, (c) MgFe ₂ O ₄ and (d) ZnO/BiOBr/MgFe ₂ O ₄ .	50
4.7	Photocatalytic activity of as-prepared samples for RhB degradation in aqueous solution. (a) Absorption spectra of RhB dyes after 180 min of sunlight exposure on ZnO/BiOBr/MgFe ₂ O ₄ ternary composite; (b) profiles of RhB photodegradation; (c) kinetic curves and (d) apparent reaction rate constants (k_{app}) obtained by applying the pseudo-first-order model.	54
4.8	Photocatalytic activity of as-prepared samples for RhB degradation in greywater. (a) Absorption spectra of RhB dyes after 180 min of sunlight exposure on ZnO/BiOBr/MgFe ₂ O ₄ ternary composite; (b) profiles of RhB photodegradation; (c) kinetic curves and (d) apparent reaction rate constants (k_{app}) obtained by applying the pseudo-first-order model.	55
4.9	Magnetic recovery of ZnO/BiOBr/MgFe ₂ O ₄ ternary composites after photocatalysis.	56
4.10	(a) Phytotoxicity of RhB dye in greywater before and after degradation using ZnO/BiOBr/MgFe ₂ O ₄ ; (b) control; (c) before degradation and (d) after degradation after 7 days.	58

LIST OF SYMBOLS/ABBREVIATIONS

θ	Diffraction angle, °
C_0	Initial concentration of pollutant at $t = 0$, mg/L
C_t	Concentration of pollutant at specific time, mg/L
E_{CB}	Conduction band minimum, eV
E_g	Band gap energy, eV
E_{VB}	Valence band minimum, eV
k_{app}	Apparent reaction rate constant, min^{-1}
t	Reaction time, min
e^-	Electrons
e_{CB}^-	Electrons at conduction band
e_{tr}^-	Trapped electrons
h^+	Holes
h_{VB}^+	Holes at valence band
h_{tr}^+	Trapped holes
h_ν	Photons
H_2O_2	Hydrogen peroxide
H_2O	Water
HO_2^\bullet	Hydroperoxyl radical
$\cdot O_2^-$	Superoxide radical
OH^-	Hydroxyl groups
$\cdot OH$	Hydroxyl radical
2D	Two-dimensional
2,4-DCP	2,4-dichlorophenol
ADMI	American Dye Manufacturer's Institute
AgI	Silver iodide
AOPs	Advanced oxidation processes
ARC	Control sample average root length

BET	Brunauer-Emmett-Teller
Bi	Bismuth
Br	Bromine
BiOBr	Bismuth oxybromide
$\text{Bi}(\text{NO}_3)_3 \cdot 5\text{H}_2\text{O}$	Bismuth nitrate pentahydrate
BOD	Biochemical oxygen demand
CB	Conduction band
CdS	Cadmium Sulfide
$\text{C}_2\text{H}_5\text{OH}$	Ethanol
$\text{C}_{19}\text{H}_{42}\text{BrN}$	CTAB chemical formula
$\text{C}_{28}\text{H}_{31}\text{ClN}_2\text{O}_3$	Rhodamine B chemical formula
CO_2	Carbon dioxide
COD	Chemical oxygen demand
CTAB	Centrimonium bromide
CuS	Copper monosulfide
DRS	Diffuse Reflectance Spectra
EDX	Energy Dispersive X-ray
Fe	Iron
Fe^{3+}	Iron (III) ion
FESEM	Field Emission Scanning Electron Microscopy
$\text{Fe}(\text{NO}_3)_3 \cdot 9\text{H}_2\text{O}$	Iron (III) nitrate nonahydrate
FTIR-ATR	Fourier Transform Infrared Spectroscopy-Attenuated Total Reflectance
GC	Gas Chromatography
GDQs	Graphene quantum dots
GMF	Gemifloxacin
GRC	Control sample germination rate
GRS	Treated sample germination rate
G_s	Germinated seeds
HPLC	High Performance Liquid Chromatography
KBr	Potassium bromide
LED	Light-emitting iodide
MB	Methylene blue

Mg	Magnesium
Mg ²⁺	Magnesium ion
MgCl ₂ ·6H ₂ O	Magnesium chloride hexahydrate
MgFe ₂ O ₄	Magnesium ferrite
MIDA	Malaysian Investment Development Authority
MnO ₂	Manganese dioxide
MO	Methyl orange
N ₀	Initial frond numbers
N ₁₀	Frond numbers after 10 days
NaOH	Sodium hydroxide
NPs	Nanoparticles
O	Oxygen
O ₂	Oxygen molecule
PL	photoluminescence
RB5	Reactive black 5
RFN	Relative Frond Number
rGO	Reduced graphene oxide
RhB	Rhodamine B
SnO ₂	Tin (IV) oxide
SS	Suspended solids
TC	Tetracycline
TiO ₂	Titanium oxide
TiO ₂ -P25	Degussa
T _s	Total number of seeds
TZR	TiO ₂ /ZnO/rGO
UK	United Kingdom
UV	Ultraviolet
UV-vis DRS	Ultraviolet-visible Diffuse Reflectance Spectroscopy
UVA	Ultraviolet A-rays
VB	Valence band
V _O	Oxygen vacancies
V _{Zn}	Zinc vacancies
WHO	World Health Organization

XRD	X-ray Diffraction
ZIF-8	Zeolitic imidazolate framework-8
Zn	Zinc
$\text{Zn}(\text{Ac})_2 \cdot 2\text{H}_2\text{O}$	Zinc acetate dihydrate
$\text{Zn}(\text{CH}_3\text{COO})_2 \cdot 2\text{H}_2\text{O}$	Zinc acetate dihydrate
Zn_i	Zinc interstitial
ZnO	Zinc oxide
ZnO-BC	ZnO-biochar
ZnS	Zinc Sulfide

CHAPTER 1

INTRODUCTION

1.1 Background of Study

Water is one of the most essential and indispensable natural resources on earth. It is incontestably the spice of life, which owns a prominent place in ensuring the continuation and sustainability of life (Chaplin, 2001). Aside from covering 71% of earth's surface (Keskin, et al., 2021), water constitutes large portion of body weight in human ranging from 75% in infants to 55% in the elderly, granting the function of cell homeostasis and metabolism (Popkin, D'Anci and Rosenberg, 2010). Nonetheless, water is limited despite its tremendous abundance, especially for freshwater. According to a statistic by the United Nations, the freshwater availability will be reduced by at least 10% for 685 million population in more than 570 cities in 2050, owing to the increase in demand of freshwater in conjunction with the rapid industrial growth (Ho, et al., 2021). Therefore, the initiatives on conservation of clean water resources are of utmost importance in order to prevent the shortage in water supply as well as retaining the biodiversity of natural ecosystem (Kilic, 2020).

Synthetic dyes had been extensively used as colorants in various industries, including textiles, paper, cosmetics, plastics, food and leather (Pathak, et al., 2011). It is permitted that approximately 7×10^5 metric tons of dyes are produced annually which could be accounted for the enormous amounts of dye effluent being discharged into water bodies without proper treatment (Agrawal and Verma, 2020). As reported by World Health Organization (WHO), textile industry had contributed 17-20% of water pollution (Ikram et al., 2020). Rhodamine B (RhB) is a cationic basic dye that belongs to anthraquinone family, which is widely employed in textiles industry, silk, wool, dye

cells in biotechnology and food products (Dao et al., 2021). However, the wastewater generated by this dye is generally depicted to be concentrated in organic pollutants, high chromaticity, and difficult to biochemically degrade as well as proclaimed to be hazardous to human (Xu and Ma, 2021). Hence, it is crucial to propose an advanced treatment technology to degrade the dye contaminants in wastewater before releasing into environment and thereby reduce water pollution.

In fact, there are various conventional water remediation technologies in the past decades including coagulation, flocculation, reverse osmosis and activated carbon adsorption, which had been devised to address the environmental issue caused by dye contaminants (Mahendran and Gogate, 2021). However, these conventional treatment methods are restricted by the limitations such as poor removal efficiency, sludge formation and secondary pollution by toxic by-products (Liu et al., 2020). Hence advanced oxidation processes (AOPs); for instance, photolysis, photocatalysis, ozonolysis, Fenton oxidation, etc., and their combinations have been proposed to further enhance the water remediation system in tertiary treatment due to the high removal efficiency and utilisation of green energy sources (Johnson, Ali and Kumar, 2019; Zhang et al., 2021). The fundamental of AOP is the in-situ generation of highly reactive oxidising radical, primarily hydroxyl radicals ($\cdot\text{OH}$) that capable of degrading persistent organic pollutants into biodegradable organic products (Zhong et al., 2021). Among the AOPs, photocatalysis is considered to be a promising approach to remove dye contaminants from effluent water as it allows the most effective decomposition, high stability, cost efficiency and environmental friendliness (Zhang et al., 2021). Photocatalysis takes place in semiconductors upon light irradiation where the photogenerated electron-hole pair reacts with the H_2O and O_2 adsorbed on the active surface, forming hydroxyl radical ($\cdot\text{OH}$) and superoxide radical ($\cdot\text{O}_2^-$), which are participating in the degradation of organic pollutants (Domínguez-Jaimes et al., 2021).

Among numerous existing semiconducting metal oxides, zinc oxide (ZnO) is regarded as a very effective and appealing photocatalytic material on account of its non-toxicity, prominent photocatalytic performance and low preparation cost (Liu et al., 2021). Nevertheless, the photocatalytic performance of ZnO is greatly constrained by its rapid recombination of charge carrier pair and limited to ultraviolet (UV) light absorption due to large band gap (Yang et al., 2021). To overcome these shortcomings, coupling with two or more narrow band gap semiconductor has been proposed as a

via a viable approach to promote the charge separation and extend the photoresponsivity to the visible light spectrum (Qamar et al., 2021). Bismuth oxybromide (BiOBr), a typical p-type semiconductor with a tetragonal matlockite structure has attracted rising attention among the researchers due to the small band gap (2.88 eV) and high sensitivity to visible light irradiation (Zarezadeh et al., 2020). The magnificent structural features of BiOBr have permitted it to be a felicitous candidate incorporated into ZnO to induce higher charge separation efficiency and elevated photocatalytic potential (Lu, Wu and Zhou, 2021). Inspired by the emerging evolution of ternary nanocomposites, for instance, Au/Ag/AgCl (Xu et al., 2021), ATO/g-C₃N₄/TiO₂ (Ojha, Karki and Kim, 2018) and ZnO/ZnS/MoS₂ (Fu et al., 2021) which exhibited greater photocatalytic performance than their corresponding binary and single semiconductors, the interests on introducing a third component have been provoked to further improve the separation of charge carrier and enhance the light absorption range of ZnO/BiOBr. Accordingly, magnesium ferrite (MgFe₂O₄) that manifested magnetocrystalline anisotropy and saturated magnetization as well as narrow band gap of 2.0 eV is among the promising photocatalytic material for construction of a p-n-n ternary heterojunction (Kumar et al., 2021).

1.2 Problem Statement

Over recent decades, extensive consumption of organic dyes in various industries such as textiles, paper and pulp, tannery and paint manufacturing has led to ubiquitous presence of dye effluents in aquatic environment, which is detrimental to biological ecosystem and human health (Zhu et al., 2019). Rhodamine B (RhB), a xanthene dye which is substantially employed as colorant and water tracer, exhibits deleterious impact to human and animal owing to its developmental and reproductive toxicity as well as carcinogenicity (Dao et al., 2021). Conventional treatment methods including biological processes, flocculation, adsorption and reverse osmosis are perceived to be inadequate for degrading dyes due to low efficiency and expensive post treatment (Cadenbach et al., 2021). Therefore, it is indispensable to develop advanced water remediation technologies to degrade RhB into less virulent substance. Photocatalytic degradation induced by solar energy has been regarded as an alternate approach for the purification of dye effluent via generation of photoexcited reactive radicals, which allows the complete breakdown of dye contaminants (Xue et al., 2020). Compared with conventional methods, photocatalysis is denoted as an environmentally friendly process with inexpensive cost, high efficiency and low secondary pollution (Al-Kahtani, 2017).

In the past few years, titanium oxide (TiO_2) and ZnO semiconductors had expanded substantially in the application of photocatalysis due to high chemical and physical stabilities as well as low cost (Lee et al., 2021). Although ZnO possesses characteristics comparable to TiO_2 , it is reported that the photocatalytic activity of ZnO is generally higher than TiO_2 owing to its better electron mobility with diminished recombination loss that allows rapid charge carrier transport (Das et al., 2021). In addition, ZnO is widely recognized as an ideal semiconductor material because of the distinct benefits such as inexpensive cost, ease of availability, non-toxic and large band gap (Liu et al., 2021). Nonetheless, the widespread application of ZnO is still severely restricted by the wide band gap of 3.37 eV that leads to low efficiency of solar energy utilization by limiting the light absorption to UV light, which accounts for only 3-8% of solar spectrum (Sa-nguanprang et al., 2020). Besides that, the rapid recombination of photoinduced electron-hole pairs that appears to be faster than surface redox reaction, also imitates as a constraining factor for ZnO, thereby resulted in low quantum yield

(Song et al., 2021). In light of these issues, it is thus persuasive to propose some adequate modifications for ZnO to enhance its properties.

To circumvent the limitation of bare ZnO, various modification techniques including metal deposition (Jyothi and Ravichandran, 2020), ion doping (Christy et al., 2021) and heterojunction nanocomposite (Girija Shankar et al., 2021) have been thoroughly investigated by the researchers for dye degradation. Among these strategies, forming a ZnO-based heterojunction nanocomposite incorporated with different semiconductors is at the lead of a strategy-driven approach that able to promote visible light absorption and induce effective charge carrier separation (Sin et al., 2019). Recent experimental studies had revealed that the photocatalytic activity of ZnO can be remarkably improved by coupling with BiOBr, owing to its superior visible light absorption and unique structure of tetragonal matlockite framework (Geng et al., 2017). The strong internal electric field generated by the $[\text{Bi}_2\text{O}_2]^{2+}$ layers interleaving with Br atom is depicted to elucidate the effective charge transfer and suppression of charge carrier from recombination upon coupling (Zhang and Zeng, 2017). However, in the case of a typical p-n junction as in ZnO/BiOBr, it is found that parts of the reduction and oxidation potential of photoinduced charge carriers are lost throughout the extent of migration toward the higher valence band (VB) and lower conduction band (CB) energy levels, resulting in poor degradation efficiency (Moradi et al., 2021). Therefore, introduction of a third component into the binary composite is vital to prevail over the aforementioned drawbacks. As a ternary n-type semiconductor, MgFe_2O_4 is known to possess distinct features such as large surface area with suitable band gap of 2.0 eV, excellent photochemical stability, high electromagnetic efficiency and strong mechanical hardness (Yuan et al., 2015; Syed et al., 2021). These properties render MgFe_2O_4 to be a reassuring candidate for coupling with ZnO/BiOBr to construct ternary heterojunction to ensure more effective separation of charge carrier and further improve the quantum efficiency for visible light spectrum (Faisal et al., 2021).

1.3 Objectives

This research project encompasses three major objectives, which are:

- i. To synthesize ZnO/BiOBr/MgFe₂O₄ ternary Z-scheme heterojunction photocatalyst via a ultrasonic-precipitation method.
- ii. To characterize the physiochemical and optical properties of as-synthesized photocatalyst.
- iii. To determine the performance of as-synthesized photocatalyst on photodegradation of Rhodamine B in both aqueous solution and grey water under sunlight irradiation.

1.4 Scope of Study

ZnO/BiOBr/MgFe₂O₄ ternary composite was synthesized via ultrasonic-deposition method and characterized with a series of characterization technique such as Field Emission Scanning Electron Microscopy (FESEM), Energy Dispersive X-ray (EDX), X-ray Diffraction (XRD), Fourier Transform Infrared Spectroscopy-Attenuated Total Reflectance (FTIR-ATR) and Ultraviolet-visible Diffuse Reflectance Spectroscopy (UV-vis DRS). Subsequently, a photocatalytic study will be conducted on the degradation of Rhodamine B (RhB) in both aqueous solution and greywater over the as-synthesized photocatalysts under sunlight irradiation, followed by phytotoxicity tests on the treated effluent.

CHAPTER 2

LITERATURE REVIEW

2.1 Review on Dye in Wastewater

In recent years, the textile sector in Malaysia had evolved expeditiously as a result of the rapid globalization expansion and industrial development, which leading to the increased demand and intensive consumption for dyes (Rasiah, 2009). As reported by the Malaysian Investment Development Authority (MIDA) in 2016, the textile sector was the tenth largest exporter earner in Malaysia with export value of RM12.6 billion, which contributed 2.6 % out of total export of manufactured goods (MIDA, 2016). However, textile industry has been perceived as the leading cause of wastewater contamination due to the discharge of dye effluents which are extremely recalcitrant and toxic (Wong et al., 2018). It is reported that approximately 80-85% of dyes are utilized in textile industries, with 15% of them being lost during the dyeing process and released to the water bodies without any further treatment (Zubair et al., 2021). The textile effluents normally comprised of approximately 10-100 mg/L of dye containing carcinogenic amines (Mustafa et al., 2021) and other chemical pollutants in the form of heavy metals (Ghaly et al., 2014), halogen carriers (Eswaramoorthi et al., 2008), free chlorine (Turhan and Turgut, 2009), biocides and softeners (Avlonitis et al., 2008). As a result, these compositions tend to give rise to water-polluting textile effluents which are high in colour, pH, temperature, suspended solids (SS), chemical oxygen demand (COD), biochemical oxygen demand (BOD), metals and salts (Yaseen and Scholz, 2018).

Accordingly, the total amount of wastewater contributed by textile industry in Malaysia had escalated dramatically from 744 tons in year 2007 to 1559 tons in year

2009, which accounted for 22% of the total industrial wastewater produced (Hanafi and Sapawe, 2020). From Figure 2.1, it should be highlighted that the primary sources of wastewater contamination generated by textile industries are mainly focused in Peninsular Malaysia with Johor state contributing the most to water pollution (28.6%), succeeded by Pulau Pinang (28.2%) and Selangor (15.6%), which could be attributed to the considerable number of textiles finishing plants located at these states (Pang and Abdullah, 2013).

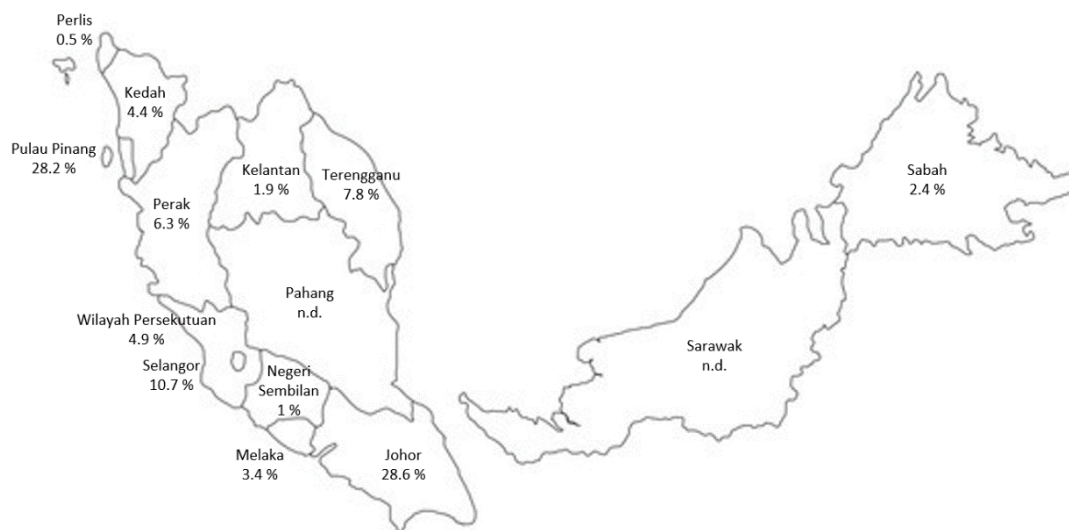


Figure 2.1: The textile industry's contribution to water contamination in several states of Malaysia (Pang and Abdullah, 2013).

Apart from the presence of dyes in textile effluent, dye contaminants can be found in greywater as well due to the leaching of dyes from household sources such as fabrics, foods and personal care products into the water system (Chong et al., 2015). Greywater, which is a source of wastewater generated from laundries, showers, kitchen sinks and washing machines constitutes about 50-80% of total domestic wastewater (Ong et al., 2019). In addition, according to the statistics done by Oh et al., it is revealed that 43% of total water usage in Malaysia ends up as greywater and producing 0.097 m³/p/d of greywater in year 2010, which is higher than the United Kingdom (UK) with volume of 0.088 m³/p/d (Oh et al., 2018). As shown in Figure 2.2, 65% of potable water in Malaysia is utilized for flushing toilets, showering and laundry washing. The

household activities including gardening, car washing, outdoor activities and household cleaning account for 20% of potable water usage while 15% of water is wasted due to pipe leakages that typically go undiscovered for long periods of time (Oh et al., 2018).

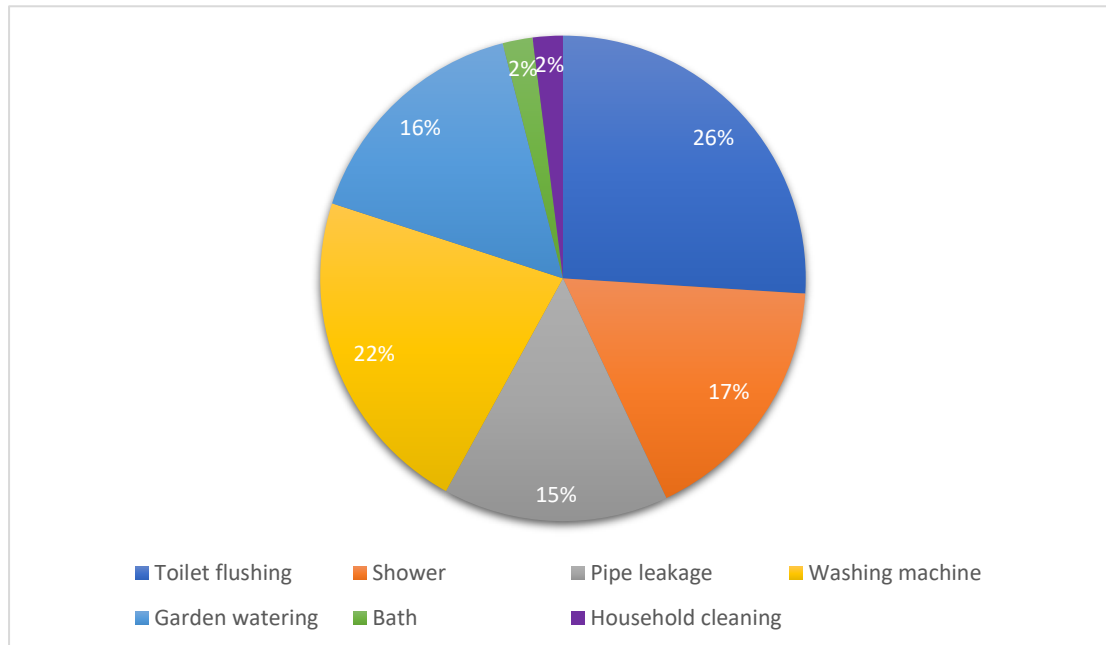


Figure 2.2: Average water usage distribution (%) in Malaysia (Oh et al., 2018).

Generally, greywater contains lesser organic pollutants than industrial effluent but its composition varies extensively depending on the lifestyle, water source quality, demographics and the type of chemicals used for household activities (Oteng-Peprah et al., 2018). The treatment of greywater not merely replenishes water resources, but in fact having lower treatment cost as compared to municipal wastewater, owing to the low contamination of grey water. Grey water can be treated using a variety of approaches, including biological (Khalil and Liu, 2021), chemical (Shreya et al., 2021), and physical methods (Kim and Park, 2021). However, the biological treatment approaches are inefficient due to the minimal organic content of grey water. Furthermore, physical treatment procedures alone cannot decrease contamination to an acceptable level for the environment (Hassanshahi and Karimi-Jashni, 2018).

The disposal of untreated greywater into water bodies poses insidious threats to the environment and ecosystem owing to the various hazardous contaminants existing in greywater such as synthetic dyes, surfactants, preservatives and solvents which could

affect the water quality parameters (Priyanka et al., 2020). Moreover, the presence of dyes in aquatic environment is readily visible even at very trace concentrations (<1 ppm), thereby causing water pollution (Rafiq et al., 2021). In reality, natural degradation processes do not eliminate dye chemicals from wastewater, but instead produces secondary hazardous by-products in natural water systems and the environment due to the high stability of complex aromatic structure in dye pollutants (Doan et al., 2020; Noman et al., 2020). Therefore, the dye pollutants in both the textile effluent and greywater are mandatory to be treated using water remediation technologies by meeting the legislative requirement in accordance with standard A and B of which the colour intensity must not exceed 100 ADMI (refer Table 2.1).

Table 2.1: Wastewater Discharge Standard (Department of Environment, 2015).

Parameter	Unit	Standard	
		A	B
(i) Temperature	°C	40	40
(ii) pH Value	-	6.0-9.0	5.5-9.0
(iii) BOD ₅ at 20°C	mg/L	20	50
(iv) Suspended Solids	mg/L	50	100
(v) Mercury	mg/L	0.005	0.05
(vi) Cadmium	mg/L	0.01	0.02
(vii) Chromium, Hexavalent	mg/L	0.05	0.05
(viii) Chromium, Trivalent	mg/L	0.20	1.0
(ix) Arsenic	mg/L	0.05	0.10
(x) Cyanide	mg/L	0.05	0.10
(xi) Lead	mg/L	0.10	0.5
(xii) Copper	mg/L	0.20	1.0
(xiii) Manganese	mg/L	0.20	1.0
(xiv) Nickel	mg/L	0.20	1.0
(xv) Tin	mg/L	0.20	1.0
(xvi) Zinc	mg/L	2.0	2.0
(xvii) Boron	mg/L	1.0	4.0
(xviii) Iron (Fe)	mg/L	1.0	5.0

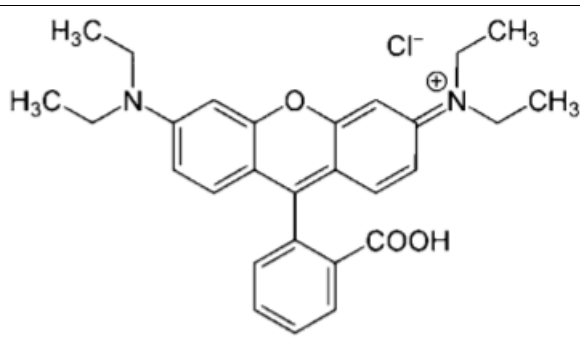
Table 2.1 Continued.

(xix) Silver	mg/L	0.1	1.0
(xx) Aluminium	mg/L	10	15
(xxi) Formaldehyde	mg/L	1.0	2.0
(xxii) Phenol	mg/L	0.001	1.0
(xxiii) Free chlorine	mg/L	1.0	1.0
(xxiv) Sulphide	mg/L	0.50	0.50
(xxv) Oil and Grease	mg/L	1.0	10
(xxvi) Ammoniacal Nitrogen	mg/L	10	20
(xxvii) Colour	ADMI	100	200

2.2 Usage and Hazardous Effects of Rhodamine B

Rhodamine B (RhB) is an organic chloride salt with N-[9-(2-carboxyphenyl)-6-(diethylamino)-3H-xanthen-3-ylidene]-N-ethylethanaminium serving as its counterion (Yamashita et al., 1998). Belong to the class of xanthene dye, it is commonly known as a basic cationic dye having high solubility in water and ethanol (Joshiba et al., 2021). The physicochemical properties of RhB are outlined in Table 2.2. It is extensively used as colorant in staining industries such as textile, wool, silk, paper, tannery and paint (Dao et al., 2021). Moreover, its photostability and photophysical properties like quantum yield and polarization allows it to be widely applied as laser dyes (Reisfeld et al., 2021) for characterization of the polymer nanoparticles surface (Fonseca et al., 2007), structure and dynamics study of micelles (Kandhasamy et al., 2021) and imaging in living cells (Vijay, Wu and Velmathi, 2019). Besides that, RhB is frequently employed as fluorescent probes for optical monitoring of pH, owing to its high photosensitivity and broad fluorescence in the visible region of electromagnetic spectrum (Battula et al., 2021).

Table 2.2: Physicochemical properties of Rhodamine B (Allé et al., 2020).

Properties	Values
Molecular structure	
Chemical formula	$C_{28}H_{31}ClN_2O_3$
Molecular weight (g/mol)	479.02
Name (CI)	Basic Violet 10
Color index (CI) number	45170
λ_{max} (nm)	554
Solubility	Very high in organic solvents (eg. water, ethanol, etc.)

Nevertheless, RhB is recognized as a highly toxic dye that poses carcinogenic, bio-recalcitrant and mutagenic behavior for any living organism (Topare, Bhutada and Bansod, 2021). Recent experimental studies had revealed the potential of RhB in affecting the human biological activity and causing water borne diseases such as nausea, hemorrhage, skin and mucous membrane ulcers, dermatitis, nasal septum perforation and respiratory tract irritation (Baldev et al., 2013). Furthermore, RhB is a major and long-term concern for aquatic life, especially plants, because it creates obstruction for light penetration into water bodies, thus disrupting the normal photosynthetic potential of aquatic flora and interfering with natural purification (Topare, Bhutada and Bansod, 2021). It is note-worthy that the color of RhB is an obvious indicator of water pollution even at low concentration, in which it capable of altering the water quality parameters including COD, BOD, pH and dissolved oxygen concentration, and subsequently influencing the biological balance of aquatic ecosystem (Hashmi et al., 2021).

2.3 Heterogeneous Photocatalysis

The craving for clean, sustainable, and renewable energy, as well as environmental remediation, has sparked a surge in research interest in photocatalysis, a robust method for capturing sunlight as the major energy source. Heterogeneous photocatalysis using various semiconductors is a sophisticated oxidation process commonly for the photo-oxidation of organic and inorganic pollutant in the fields of air cleaning and water purification (Khataee and Fathinia, 2013). The mechanism of heterogeneous photocatalysis is contingent on the fundamental of charge carrier generation upon light irradiation to initiate reduction and oxidation reactions on the surface of semiconductor (Ahmed and Haider, 2018). Semiconductors (e.g., TiO_2 , ZnO , ZnS , CdS etc.) exhibits unique electronic structure composed of a completely occupied valence band (VB) and an empty conduction band (CB), which allow them to act as sensitizer of light induced oxidation processes (Saha, 2012). In particular, the absorption of a photon with energy equal to or higher than the band gap energy (E_g) activates the semiconductor, resulting in the migration of an electron (e^-) from the VB to the CB, followed by simultaneous creation of a positive hole (h^+) in the VB. These electron-hole pairs may recombine by re-emitting energy in the form of heat or light, or the charge carrier can induce redox reactions with species adsorbed on photocatalyst surface (Vaiano, Sannino and Sacco, 2020).

Extensive research has been conducted over the last few decades to investigate improved photocatalysts with superior light harvesting capabilities, high charge carrier separation efficiency, and efficient catalytic reactivity for optimizing the conversion efficiency of solar energy (Gao et al., 2020). Fundamentally, three key factors predominantly dictate the overall efficiency of a photoactive semiconductor: (i) band gap (E_G); (ii) band position; and (iii) bulk and surface charge carrier dynamics such as diffusion length, mobility, charge lifetime and recombination rate (Thomson, Lee and Vilela, 2020; Tan, Abdi and Ng, 2019). The schematic of the key aspects is depicted in Figure 2.3. In overall, E_G is described by the energy difference between valence band minimum (E_{VB}) and conduction band minimum (E_{CB}), which restrains the portion of solar spectrum for activation of semiconductor. For instance, the photosensitivity of semiconductors with E_G more than 3 eV is merely limited to the UV light absorption in which the semiconductors with a smaller bandgap are conducive to more proficient solar energy harvesting (Ibhadon and Fitzpatrick, 2013). On the other hand, the

reducing and oxidizing powers of the photoinduced electron-hole pair is defined by the E_{CB} and E_{VB} potentials of semiconductor. From the thermodynamic point of view, the adsorbed electron acceptor species can only be reduced by higher E_{CB} potential (more negative), while the oxidation reaction at VB can only occur if the E_{VB} potential is lower (more positive) than the oxidation potential of the adsorbed electron donor (Augugliaro et al., 2019). The kinetics of photogenerated electrons and holes are equivalently dominant for determination of the number and efficiency of charge carriers that remain active for participating in the interface reaction at the semiconductor/solution phase boundary (Byrne et al., 2015).

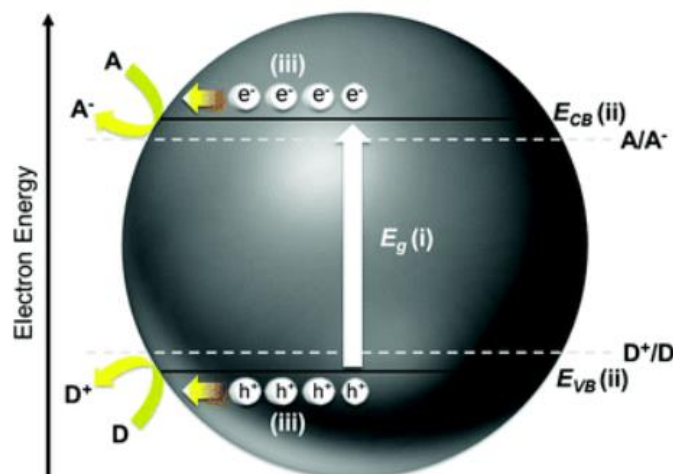


Figure 2.3: Schematic illustration of the key aspects governing the photocatalytic activity of semiconductor (Tan, Abdi and Ng, 2019).

2.4 ZnO as Photocatalyst

ZnO is a II–VI compound semiconductor that possesses large ionicity residing at the borderline between covalent and ionic semiconductors. It is recognized by having a tetrahedral coordination with typical sp^3 covalent bonding nature and substantial ionic character, which contribute to the large bandgap energy (Morkoç and Özgür, 2009). In general, ZnO can form three crystal structures: hexagonal wurtzite, cubic zincblende and rocksalt as shown in Figure 2.4. Under ambient circumstances, the hexagonal wurtzite form of ZnO is the most common and thermodynamically stable phase, whereas the zinc blende structure can only be maintained by growing ZnO on cubic substrates, and ZnO occurs in rocksalt form only at relatively high pressures. (Ong, Ng and Mohammad, 2018). ZnO is an inherently n-type semiconductor characterized by the presence of intrinsic defects such as oxygen vacancies (V_O), zinc vacancies (V_{Zn}) and zinc interstitial (Zn_i), which result in various optical and electrical properties (Boukos, Chandrinou and Travlos, 2012). It is reported that a greater V_O and V_{Zn} can enhance the photocatalytic performance of ZnO significantly by creating an intermediate energy level near the valence band, which able to induce band gap narrowing and thereby promoting visible light absorption. Moreover, the presence of V_O on the surface of ZnO is proved to be responsible for the suppression of photoinduced charge carrier by behaving as electron traps (Le et al., 2020).

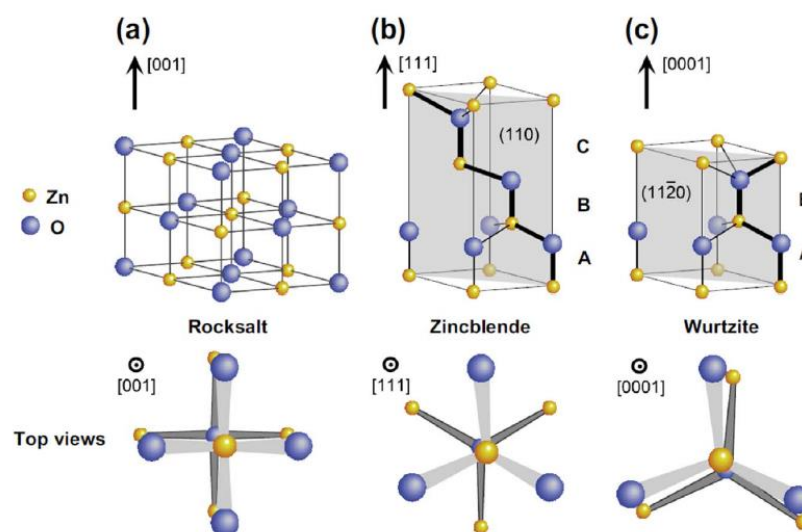


Figure 2.4: Stick and ball representation of ZnO crystal structures: (a) cubic rocksalt, (b) cubic zincblende and (c) hexagonal wurtzite (Ong, Ng and Mohammad, 2018).

For the past few decades, intensive research had been conducted to evaluate the viability of ZnO as an alternative photocatalyst to TiO₂, with the findings suggested that ZnO presents an overall better photocatalytic behavior than TiO₂ in pollutant degradation. For instance, Han *et al.* (2012) studied the effect of catalyst loading on degradation efficiency of estrone using ZnO and TiO₂ under artificial UVA irradiation. Their results revealed that 95% degradation of estrone was achieved within 45 min at catalyst loading of 0.01 g L⁻¹ ZnO, while TiO₂ only able to degrade 70% of estrone provided the similar reaction condition. In overall, the photocatalytic degradation of estrone by ZnO at all catalyst loadings was revealed to be more superior to that of TiO₂ under artificial UVA or solar irradiation, which could be ascribed to the ionic defects in ZnO (positively charged interstitials and oxygen vacancies) that allow the trapping of charge carriers and thus facilitate the redox reactions by impeding the recombination of photoinduced electron-hole pairs. Besides, Kansal, Singh and Sud (2007) had conducted another comparative study for photocatalytic degradation of methyl orange (MO) and rhodamine 6G (R6G) using various semiconductors such as ZnO, TiO₂, SnO₂, ZnS and CdS. The results indicated that the photocatalytic performance of ZnO is the highest among all the selected semiconductors at different pH values by exhibiting the decolorization efficiency of up to 98% for both dyes. This could be explained by the higher quantum efficiency of ZnO as compared to TiO₂ and others due to its suitable band gap and band position.

Moreover, an experimental study for degrading phenol using ZnO and TiO₂ in the presence of manganese dioxides (MnO₂) by Li *et al.* (2008) suggested that the degradation efficiency of phenol using ZnO was relatively higher (95%) than TiO₂ (90%) in 150 min of UV irradiation. In addition, it was found that the presence of coexisting inorganic ion like MnO₂ in wastewater, even in trace amounts, can impede the photocatalytic performance of TiO₂ significantly in contrast to the slight decline in photocatalytic activity of ZnO. These results implied the enhanced removal efficiency of phenol and excellent stability of ZnO as a reliable photocatalyst. On the other hand, Tian *et al.* (2012) investigated the photodegradation of methyl orange (MO) using ZnO semiconductors synthesized via calcination of zinc acetate dihydrate (Zn(Ac)₂•2H₂O) and TiO₂-P25 (Degussa). Their findings concluded that the degradation rate using the ZnO catalyst was four times higher than that for Degussa TiO₂-P25 catalyst, with degradation efficiency of 100% in 120 min under UV light illumination. The enhanced

photocatalytic performance of ZnO could be ascribed to its high specific surface area and crystallinity which increased the adsorption capacity for organic pollutants. Notably, the photocatalytic efficiency of ZnO calcined at 600°C (ZnO-600) shows no visible change (remain at 100%) after five recycles, suggesting its decent reusability.

Table 2.3: Photocatalytic activity of ZnO on various pollutant

Pollutant	Synthesis method	Light source	Process condition	Best condition	Performance	Reference
Estrone	ZnO commercial (wurtzite type),	18 W UVA lamp (320-400 nm)	$C_o = 20$ ppm, Dosage = 0.01-1.0 g/L	Dosage = 0.5 g/L, $k = 362 \times 10^{-3}/\text{min}$	95% at 10 min	(Han et al., 2012)
Methyl orange/ Rhodamine 6G	ZnO commercial	30 W UV lamp (365 nm)	$C_o = 5$ -200 mg/L, Dosage = 0.25-2.0 g/L, pH = 2-10	$C_o = 25$ mg/L, Dosage = 1 g/L, pH = 8/ $C_o = 25$ mg/L, Dosage = 0.5 g/L, pH = 10	98% at 4 hr/98 % at 3 hr	(Kansal, Singh and Sud, 2007)
Phenol	ZnO commercial	70 W high-pressure mercury UV lamp (365 nm)	ZnO, ZnO/ β -MnO ₂ , ZnO/ γ -MnO ₂ , ZnO/ δ -MnO ₂ , $C_o = 20$ mg/L, Dosage = 200 mg/L, $C_{MnO_2} = 20$ mg/L, pH 6, 25°C	ZnO > ZnO/ β -MnO ₂ > ZnO/ γ -MnO ₂ > ZnO/ δ -MnO ₂	95%/91%/90%/80% at 150 min	(Li et al., 2008)

Table 2.3 Continued.

Methyl orange	Direct pyrolysis	30 W UV lamp (365 nm)	ZnO-400, ZnO-600, ZnO-800, ZnO-900	ZnO-600 > ZnO-800 > ZnO-400 > ZnO-900, $k = 12.5 \times 10^{-3}/\text{min}$	100%/98%/84%/57% at 120 min	(Tian et al., 2012)
Congo red	Hydrothermal	Solar irradiation	$C_o = 5\text{-}20$ ppm, Dosage = 0.05-0.20 g, pH = 3-11	$C_o = 5$ ppm, Dosage = 0.171 g, pH = 6.43	96% at 180 min	(Yashni et al., 2021)

2.5 Mechanism of ZnO Photocatalysis

ZnO is a promising semiconductor with a broad direct bandgap width (3.37 eV), a high excitation binding energy (60 meV) and deep violet/borderline UV absorption (Ong, Ng and Mohammad, 2018). The photocatalysis of ZnO can be elucidated by the following mechanism: charge carrier generation, trapping, charge recombination and interfacial charge transfer.

Charge carrier generation

When ZnO is subjected to solar irradiation with photonic energy ($h\nu$) equal to or higher than the excitation energy (E_g), the electrons (e^-) in the filled valence band (VB) are promoted to a vacant conduction band, leaving holes in VB and thereby resulting in the formation of electron-hole pairs (Albiss and Abu-Dalo, 2021) as shown by Eq. (2.1).



Charge carrier trapping

The photoinduced electron-hole pairs can be ensnared by the scavengers in bulk or move to photocatalyst surface and trapped there for subsequent redox reaction (Eq. (2.2) and (2.3)). In general, it is preferable to have surface trapping at either the subsurface or the surface region to hinder the charge carrier recombination in semiconductor. During the trapping stage, the primary states for charge carriers are trapped holes, trapped electrons, and free electrons (Qian et al., 2019).



Charge carrier recombination

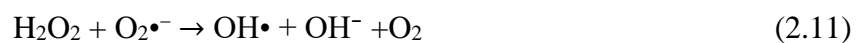
During charge transfer, there are chances for a substantial number of charge carriers (e^-/h^+ pairs) recombining quickly at the surface and interior of the bulk material, dissipating the absorbed energy in the form of light (photon production) or heat (lattice

vibration), as depicted by Eq. (2.4). For that reason, these charge carriers are unable to take part in the succeeding photocatalytic processes, which is inimical to the entire process (Kang et al., 2019). Therefore, elimination of the crystal defects is considered to be an effective route to hinder charge recombination since most of the recombination process is usually occurring at the defect sites (e.g., interstitial atoms, vacancies and grain boundaries) as reported by Qian et al. (2019).



Interfacial charge transfer

As suggested by Fagier (2021), the electron-hole pairs that migrate successfully to the surface of the semiconductor without recombining can proceed to initiate the redox reaction. The positive holes in VB react with adsorbed water (H₂O) and hydroxide ions (OH⁻) to form powerful hydroxyl radicals via oxidation reaction (Eq. (2.5) and (2.6)). The electrons in CB reduce the dissolved oxygen species into superoxide radical anions (O₂^{•-}) and hydroperoxyl radical (HO₂[•]), which will subsequently produce hydrogen peroxide (H₂O₂) as represented by Eq. (2.7), (2.8) and (2.9). The H₂O₂ will undergo a series of reaction with e⁻ and O₂^{•-} radicals to generate hydroxyl radicals (OH[•]), which may react with pollutants adsorbed on the surface of ZnO to form intermediate products that can be converted into green chemicals like CO₂, H₂O, and mineral acids afterwards (Eq. (2.10)–(2.13)).



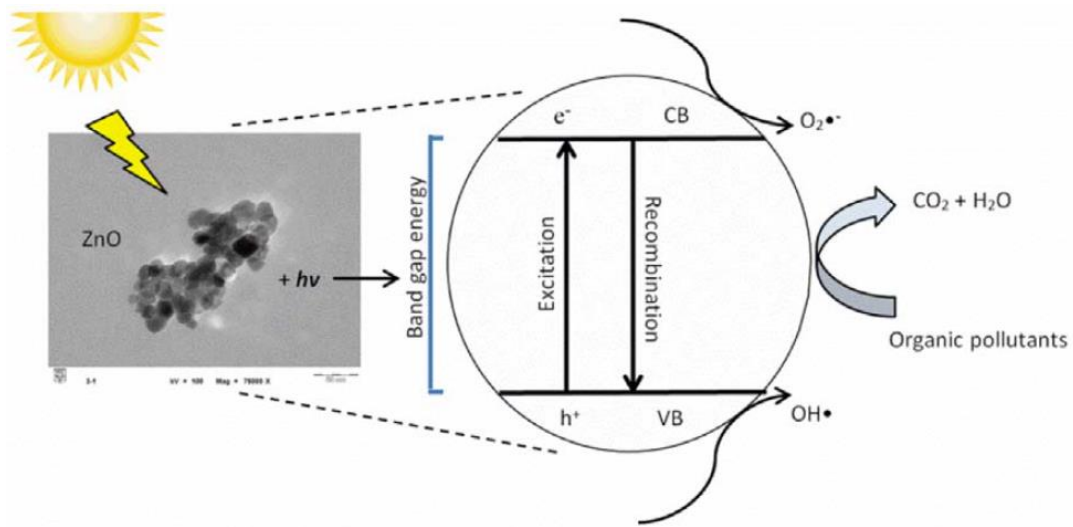
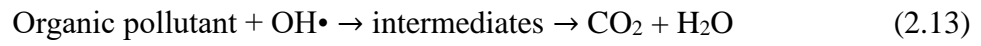


Figure 2.5: Degradation of organic pollutant by ZnO under solar irradiation (Ong, Ng and Mohammad, 2018).

2.6 ZnO/BiOBr/MgFe₂O₄ ternary Z-scheme nanocomposite

Despite the fact that ZnO is a low cost and environmentally friendly photocatalyst with potentially high photocatalytic properties, there are still a few limitations that hinder its performance as an efficient semiconductor photocatalyst including broad band gap and quick recombination of electron-hole pairs (Długosz, Szostak and Banach, 2019). Recent experimental studies had demonstrated several approaches including filling with noble metals (Vaiano et al., 2019), doping with metal and non-metals (Moiz et al., 2021), creating heterostructures with narrow band gap semiconductor materials (Bai et al., 2021), and fabricating unique nanostructures (Dey, Das and Kar, 2021) to extend the photoresponsivity of ZnO towards the visible light region in the solar spectrum as well as to improve the charge separation efficiency. Within the context of the preceding, implementing narrow band-gap semiconductor coupling to fabricate heterojunction interface has been regarded as a relatively effective approach, in which the use of semiconductors with appropriate energy band structures to construct Zscheme heterojunctions can circumvent the deficiency of conventional type-I and type-II heterojunctions (Song et al., 2021).

Bismuth oxide bromide (BiOBr) is a layered oxide semiconductor photocatalyst that consists of $[\text{Bi}_2\text{O}_2]^{2+}$ slabs sandwiched by double halide anion layers, which had received a lot of interest in a variety of applications because of its wide visible-light response range, high chemical stability, and appropriate band location (Wang et al., 2021). It shows excellent photocatalytic performance and high stability due to the unique tetragonal lattice structure that able to form intrinsic built-in electric fields, which enhance the suppression of e^-/h^+ pairs recombination significantly and induce high charge mobility (Dai et al., 2021). On the other hand, BiOBr with narrow bandgap of 2.7 eV is revealed capable of utilizing visible light to generate reactive oxygen species (ROS) through oxygen activation. In addition, it is known to possess exceptional physicochemical stability against light or water corrosion even under high/low pH conditions, which makes it to be one of the potential candidates to couple with ZnO to form heterojunction (Tu et al., 2021). However, it is discovered that parts of the reduction and oxidation potential of photoinduced charge carriers are lost throughout the extent of migration toward the higher valence band (VB) and lower conduction band (CB) energy levels in the case of a typical p-n junction like ZnO/BiOBr, which caused deterioration in photocatalytic performance (Moradi et al.,

2021). Therefore, introduction of a third component into the binary composite is vital to prevail over the aforementioned drawbacks.

Lately, the spinel ferrites family, for instance, ZnFe_2O_4 , MgFe_2O_4 and CuFe_2O_4 have attracted enormous attention in the field of water splitting and eliminating pollutants, owing to their low costs, remarkable band topologies and environmentally benign constituent elements (Wang et al., 2020; Syed et al., 2021; Janani et al., 2021). Among them, magnesium ferrite (MgFe_2O_4) is an n-type semiconductor with a relatively narrow bandgap (2.0 eV) that endows the absorption of a large portion of visible light (Yuan et al., 2015). The distribution of Mg^{2+} and Fe^{3+} cations between tetrahedral (A) and octahedral [B] sites of spinel structure render it to own superior magnetic, electrical and optical properties (Garcia-Muñoz et al., 2019). As a magnetic material, MgFe_2O_4 has a high magnetism and excellent chemical stability in acid and base media, which allow it to be readily recovered from aqueous suspension by applying an external magnetic field (Jiang et al., 2020). Heidari and Masoudpanah (2020) reported that the coupling of ZnO with MgFe_2O_4 can further enhance the saturation magnetization of the heterostructure due to the imbalance of Fe^{3+} cations between (A) and [B] sites resulted from tuning effect, which give rise to higher efficiency of charge separation. Analogously, the visible light harvesting ability is expanded as well due to the well-matched band structure and thus enhancing the photocatalytic activity.

Till the present, there is no report regarding the combination of ZnO, BiOBr and MgFe_2O_4 for construction of heterojunction ternary composite. However, recent research on ZnO-based photocatalysts has focused on the construction of ternary systems as they all demonstrated exceptional photocatalytic activity than their corresponding single and binary component photocatalysts (Yang et al., 2021). For instance, Zarezadeh *et al.* (2020) synthesized a novel p-n-p BiOBr/ZnO/BiOI ternary heterostructure to investigate its photocatalytic performance in degrading various pollutants under visible light. The results demonstrated that the BiOBr/ZnO/BiOI photocatalyst displayed better degradation efficiency (99%) of RhB as compared to the pristine ZnO (16%) after 90 min of light irradiation. In addition, the rate constant of the BiOBr/ZnO/BiOI (20%) sample for removal of RhB was greater than those of the ZnO, ZnO/BiOBr (30%), ZnO/BiOI (20%) photocatalysts, which are almost 59, 3.5 and 3.8 folds larger. Based on their UV-Vis DR spectra result, the ternary heterostructure was

found to exhibit larger visible-light absorption than the single and binary structure, which could be explained by the strong interfacial coupling of ZnO with BiOBr and BiOI, as narrow band gap semiconductors. Besides, the photoluminescence (PL) spectra revealed that the ternary sample has a significantly lower PL intensity than the pure and binary photocatalysts, indicating that the charge carriers lifetime in the ternary nanocomposite is relatively longer and more likely to participate in the photocatalytic process, resulting in improved degradation efficiency.

On the other hand, Nandi and Das (2021) developed ZnO/CdS/CuS ternary heterostructure for the degradation of RhB and MO by embedding CdS and CuS nanoparticles onto the surface of micron-sized ZnO hexagonal discs via a simple low temperature aqueous solution method. In their findings, the photocatalytic efficiencies for pristine ZnO, ZnO/CdS and ZnO/CdS/CuS under 120 min of light irradiation were revealed to be 52, 72.4 and 82% for RhB, and 73.5, 88.5 and 97% for MO dye, respectively, suggesting higher photocatalytic performance of ZnO/CdS/CuS ternary photocatalyst as compared to ZnO/CdS and pristine ZnO. This may be ascribed to the ternary structure's increased specific surface area as revealed in their Brunauer-Emmett-Teller (BET) results, which resulted in enhanced adsorption capacity as well as a reduced recombination rate of photogenerated carriers via the creation of a larger heterojunction interface. Besides, they also deduced from the Diffuse Reflectance Spectra (DRS) and PL analysis results that the anchoring of CdS/CuS nanoparticles on ZnO was able to greatly improve the visible light utilization efficiency and achieve lowest charge carrier recombination rate through facilitated charge separation and transportation. Similarly, Wang *et al.* (2019) constructed a direct Z-scheme g-C₃N₄/Zn₂SnO₄N/ZnO ternary heterojunction according to the band bending theory, which was prepared using a simple UV light irradiation method. The prepared g-C₃N₄/Zn₂SnO₄N/ZnO composite exhibited improved photocatalytic activity for RhB photodegradation with higher degradation efficiency up to 98% as compared to pure ZnO (30%) and g-C₃N₄/Zn₂SnO₄N (80%). They reported that the interstitial N atoms existing in ternary heterostructure can cause asymmetric charge distribution, which will induce the formation of build-in polarization electric field that lead to strong redox ability, effective separation and rapid interfacial transfer of photoinduced electron-hole pairs.

Table 2.4: Photocatalytic activity of ZnO-based ternary nanocomposite on various pollutants.

Ternary composite	Pollutant	Preparation method	Light source	Process condition	Degradation efficiency	Reference
BiOBr/ZnO/BiOI	Rhodamine B	Hydrothermal	50 W LED lamp	$C_o = 5$ mg/L, Dosage = 100 mg	99% in 90 min	(Zarezedah, 2021)
ZnO/CdS/CuS	Rhodamine B/methyl orange	Hydrothermal	400 W metal halide lamp	$C_o = 10$ mg/L, Dosage = 5 mg	82%/97% in 120 min	(Nandi and Das, 2021)
g-C ₃ N ₄ /Zn ₂ SnO ₄ N/ZnO	Rhodamine B	UV light irradiation method	500 W xenon lamp	$C_o = 5$ mg/L, Dosage = 50 mg	98% in 60 min	(Wang et al., 2019)
ZnO/AgBr/Ag ₂ CrO ₄	Rhodamine B	Hydrothermal	50 W LED lamp	$C_o = 25$ mg/L, Dosage = 100 mg	99% in 180 min	(Pirhashemi and Yangjeh, 2015)
ZnO/AgI/Ag ₂ CO ₃	Rhodamine B	Coprecipitation	50 W LED lamp	$C_o = 10$ mg/L, Dosage = 100 mg	98% in 120 min	(Nonakaran and Yangjeh, 2016)
ZnO/BiVO ₄ /Co ₃ O ₄	Brilliant green	Hydrothermal	300 W Xenon lamp	$C_o = 10$ mg/L, Dosage = 200 mg	99.1% in 60 min	(Zhang and Xie, 2021)

2.7 Phytotoxicity

Phytotoxicity is referred to as a delay of seed germination, suppression of plant development, or any detrimental impacts on plants induced by particular compounds or growing circumstances (Blok et al., 2008). Direct discharge of various pollutants, particularly dye effluents into water bodies without sufficient treatment poses a significant environmental and health concern in which some of the contaminants degraded by photocatalysis may generate intermediate products that are more precarious than the parent pollutants (Naraginti and Yong, 2019). Therefore, it is crucial to perform phytotoxicity tests to examine the impact of irradiated solution release to the environment and evaluate the potential usage of the pre-treated aqueous solution in the irrigation field (Elghniji et al., 2012).

Khan *et al.* (2021) conducted a research study on the photodegradation of reactive black 5 (RB5) dye using graphene quantum dots (GDQs) and iron co-doped TiO₂ photocatalysts as well as evaluating their phytotoxicity. The phytotoxicity of TiO₂-300, 0.1Fe-TiO₂-300 and GDQ-0.1Fe-TiO₂-300 was assessed based on the germination of *L. esculentum* seed. With RB5 dye solution acting as the control, germination (%) was calculated using the following Eq. (2.14):

$$\text{Germination (\%)} = \frac{G_s}{T_s} \times 100 \quad (2.14)$$

Where G_s and T_s represent germinated seeds and total number of seeds, respectively. Figure 2.6 depicts the results of seed germination. It showed that the seed germination was not affected much by the types of photocatalyst, with TiO₂-300, 0.1Fe-TiO₂-300 and GDQ-0.1Fe-TiO₂-300 displaying 67%, 73% and 81.43%, respectively. The treated solution using GDQ-0.1Fe-TiO₂-300 exhibited higher seed germination than the dye solution treated with TiO₂-300 and 0.1Fe-TiO₂-300, suggesting the effectiveness of GDQ-0.1Fe-TiO₂-300 in decolorizing RB5. Further experimental findings also revealed that the control experiments with only RB5 showed relatively low seed germination (46%) as compared to treated water and photocatalysts containing water.

Gholami *et al.* (2019) investigated the sonocatalytic activity of ZnO-biochar (ZnO-BC) in degradation of gemifloxacin (GMF) and phytotoxicity tests were carried out on water, GMF solution and treated GMF solution by using *Lemna minor*. The

Relative Frond Number (RFN) was determined using Eq. (2.15) to compute the pollutant phytotoxicity.

$$\text{Relative Frond Number (RFN)} = \frac{(\text{Frond } N_{10} - \text{Frond } N_0)}{\text{Frond } N_0} \quad (2.15)$$

Where N_0 and N_{10} is the frond numbers at the beginning and after 10 days, respectively. The RFN for water, treated GMF solution, and untreated GMF solution was measured as 1.44, 1.24, and 0.16, respectively. These findings indicate that the toxicity of GMF solution is significantly higher than that of the other samples. The RFN of GMF solution increases from 0.16 to 1.24 after treatment with US/ZnO-BC process, implying a decrease in toxicity. It should be noted that the solutions with higher toxicity have lower pigment levels due to the death of the plants. The phytotoxicity of GMF solution is demonstrated by the reduced pigment level. They concluded that the US/ZnO-BC method produced low hazardous by-products and products, owing to the significant increase in the pigment concentration after GMF degradation.

Another experimental study was done by Wei *et al.* (2021) to discuss the capability of $\text{Ag}_3\text{PO}_4/\text{NrGO}/\text{CuFe}_2\text{O}_4$ photocatalyst in detoxifying 2,4-dichlorophenol (2,4-DCP). They evaluate the phytotoxicity of *V. radiata* by determining the germination index (GI) using the following equation:

$$\text{Germination Index (GI)} = \frac{\text{GRS} \times \text{ARS}}{\text{GRC} \times \text{ARC}} \times 100\% \quad (2.16)$$

In which GRS = treated sample germination rate; ARS = treated sample average root length; GRC = control sample germination rate; ARC = control sample average root length. According to their findings, the pure 2,4-DCP significantly inhibited *V. radiata* germination (only 30%), while distilled water (control) and intermediate products had no effect on their germination (100%). This essentially proved that no hazardous chemicals were produced during the breakdown of 2,4-DCP. Additionally, 2,4-DCP toxicity had a significant impact on the growth of *V. radiata* roots and shoot lengths by resulting in only a minor amount of growth. However, substantially longer root and shoot lengths were detected in seeds treated with intermediate products, confirming the detoxification of 2,4-DCP. In addition, the GI of 2,4-DCP before and after degradation were found to be 11.97% and 80.31% respectively, revealing the capacity of $\text{Ag}_3\text{PO}_4/\text{NrGO}/\text{CuFe}_2\text{O}_4$ to effectively detoxify 2,4-DCP and gives new insights on the safety discharge of chlorophenols solutions after wastewater remediation.

CHAPTER 3

METHODOLOGY

3.1 Overall Flowchart of Work

Figure 3.1 depicts a flowchart of the overall research methodology.

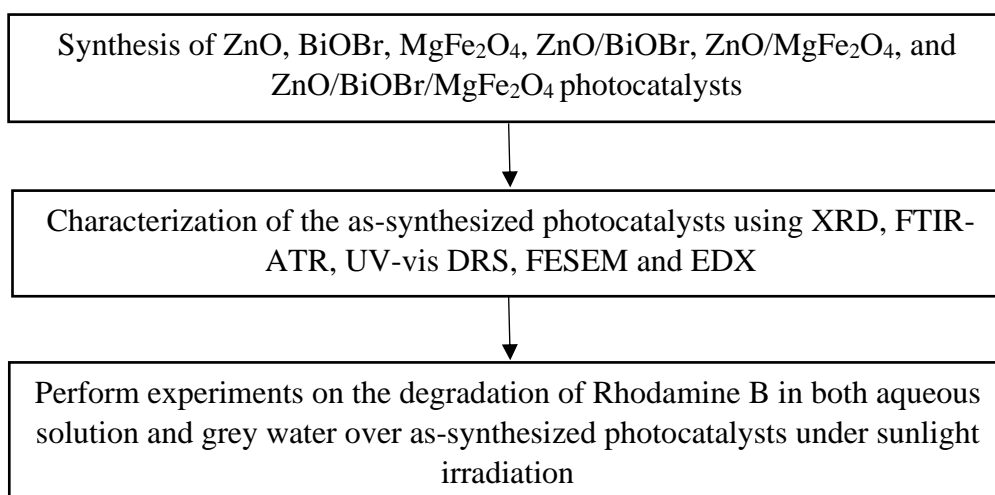


Figure 3.1: Flowchart of Overall Experimental Study

3.2 Materials and Chemicals

Table 3.1 shows the materials and chemicals that were used in this research study.

Table 3.1: List of materials and chemicals used

Material/Chemical	Purity	Supplier/Source	Application
Zinc acetate dihydrate [Zn(CH ₃ COO) ₂ .2H ₂ O]	99%	ChemSoln	Zinc precursor
Bismuth nitrate pentahydrate [Bi(NO ₃) ₃ .5H ₂ O]	98%	SYNERLAB	Bismuth precursor
Potassium bromide [KBr]	99%	SCR	Bromide precursor
Centrimonium bromide/CTAB [C ₁₉ H ₄₂ BrN]	98%	R&M Chemicals	Surfactant
Iron (III) nitrate nonahydrate [Fe(NO ₃) ₃ .9H ₂ O]	98.2%	Bendosen	Iron precursor
Magnesium chloride hexahydrate [MgCl ₂ .6H ₂ O]	99.5%	QReC	Magnesium precursor
Sodium hydroxide [NaOH]	98%	Acros Organics	pH adjustor
Ethanol [C ₂ H ₅ OH]	99.8%	ChemSoln	Solvent for photocatalyst fabrication
Distilled water	-	Gainson Advanced Technology	Solvent for photocatalyst fabrication
Rhodamine B	90%	Merck Millipore	Target pollutant

3.3 Photocatalyst Fabrication

To prepare pure ZnO, 4 mmol $\text{Zn}(\text{CH}_3\text{COO})_2 \cdot 2\text{H}_2\text{O}$ was dispersed in 60 mL ethanol and mechanically stirred for 3 hours. On the other hand, 60 mmol NaOH was dissolved into 100 mL ethanol and subjected to constant stirring for 3 hours. Then, the solution containing $\text{Zn}(\text{CH}_3\text{COO})_2 \cdot 2\text{H}_2\text{O}$ was added drop by drop into the alkaline solution under continuous stirring for 1 hour. The resulting solution was transferred to a Teflon-lined autoclave and heated at 150°C for 20 hours. The as-formed precipitates were filtered and washed with deionized water and ethanol for several times. Subsequently, the collected sample was dried in an oven at 60°C for 12 hours and grinded into fine powder using pestle and mortar. Finally, the powder was calcined in a muffle furnace at 450°C for 2 hours to obtain pure ZnO. The preparation process of ZnO is illustrated in Figure 3.2.

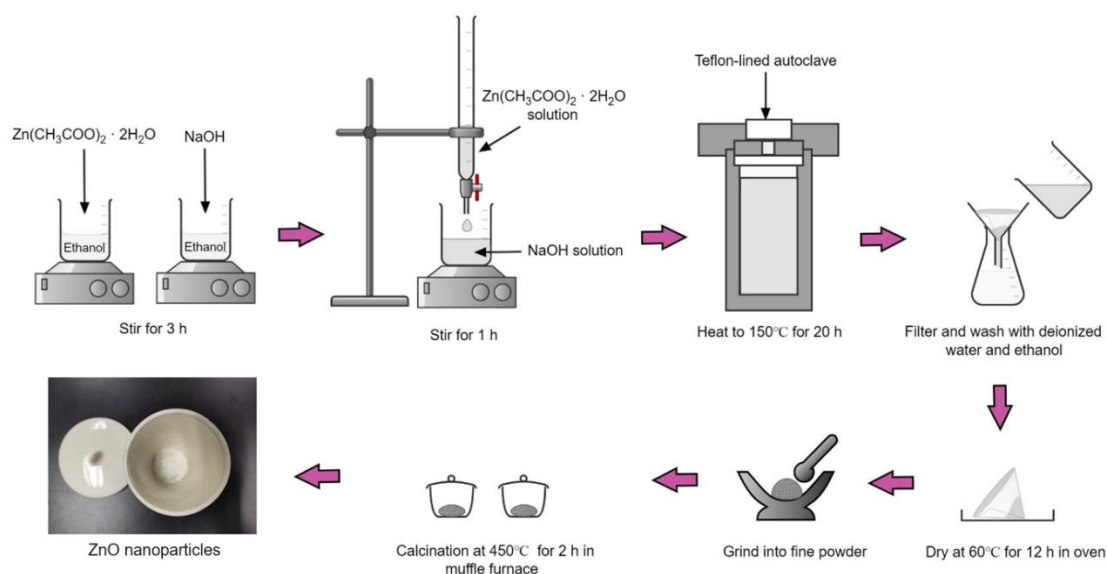


Figure 3.2: Illustration of ZnO preparation

To synthesize pure BiOBr, 5 mmol $\text{Bi}(\text{NO}_3)_3 \cdot 5\text{H}_2\text{O}$ and 5 mmol KBr were dispersed in 150 mL water for 30 minutes and subsequently stirred for 2 hours under room temperature. The resulting solution was transferred to a 200 mL Teflon-lined stainless-steel autoclave, subjected to heating at 130°C for 12 hours and left to cool overnight. The as-formed precipitates were filtered and cleansed with distilled water

for 5 times. After washing, the solid precipitates were placed in an oven and dried for 24 hours at 80°C. Then, the dried solids were grounded into fine powder and finally calcined in a muffle furnace at 450°C for 2 hours. The fabrication of pure BiOBr is shown schematically in Figure 3.3.

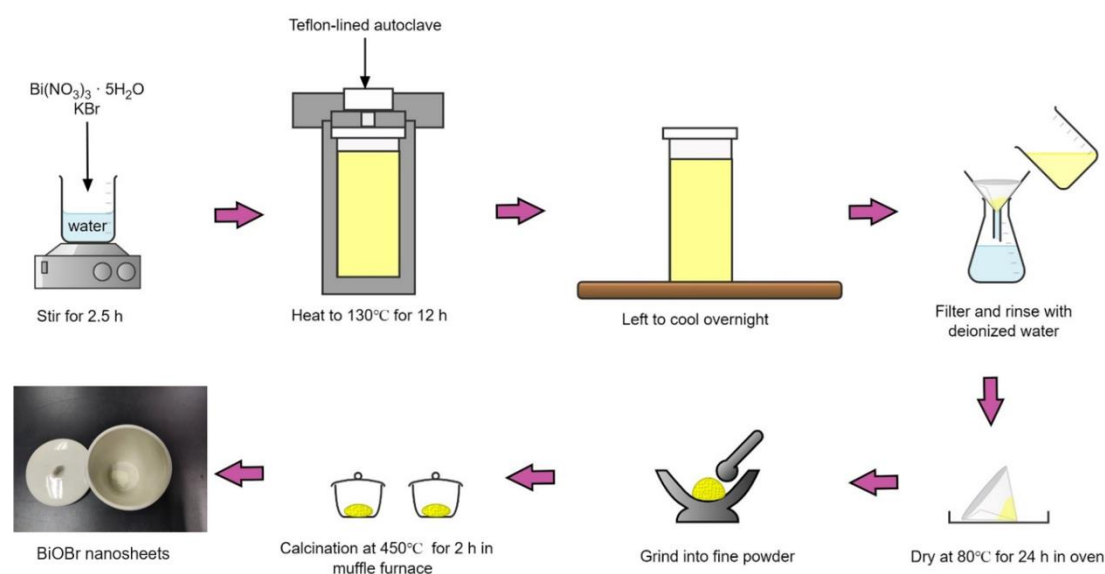


Figure 3.3: Synthesis of BiOBr nanoparticles

For preparation of pure MgFe_2O_4 , 0.1 g CTAB was dissolved in 100 mL water containing 60 mmol NaOH and subjected to stirring for 1 hour to form solution A. Subsequently, 8 mmol $\text{Fe}(\text{NO}_3)_3 \cdot 9\text{H}_2\text{O}$ and 4 mmol $\text{MgCl}_2 \cdot 6\text{H}_2\text{O}$ were added into 100 ml water and stirred for 1 hour to form solution B. Then, the solution B was added dropwise into the solution A at 80°C and stirred continuously for 2 hours. The resulting precipitates was filtered and washed with deionized water for several times. Finally, the collected sample were put into a petri dish and dried at 60-80°C for 12 hours, grinded into fine powders and eventually calcined at 450°C for 2 hours in a muffle furnace. Figure 3.4 shows the preparation method of pure MgFe_2O_4 .

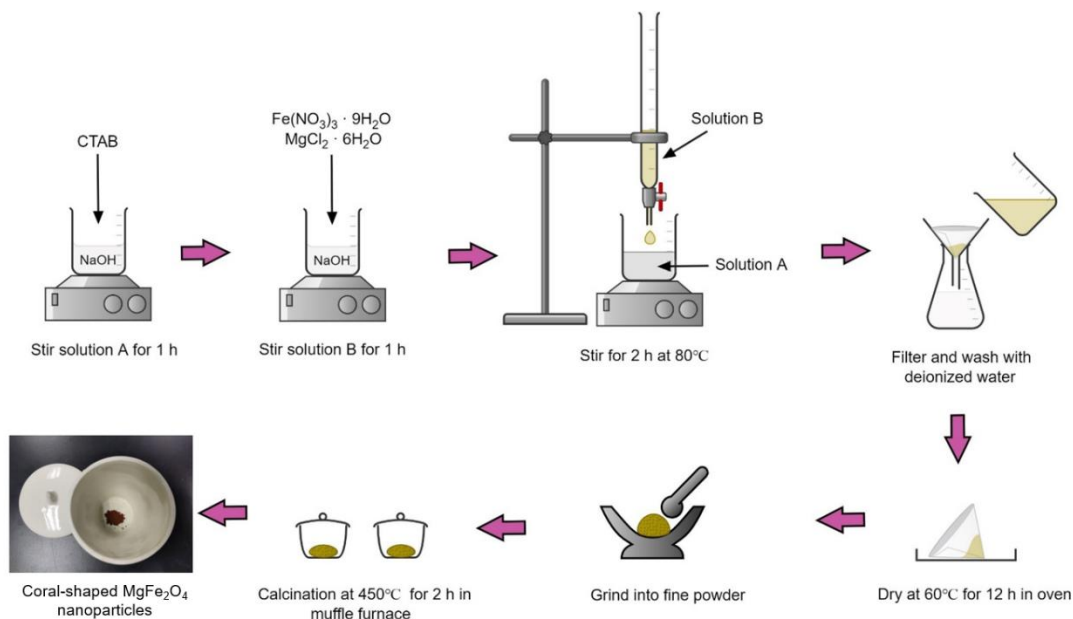


Figure 3.4: Preparation route of MgFe_2O_4 nanoparticles

The $\text{ZnO}/\text{BiOBr}/\text{MgFe}_2\text{O}_4$ nanocomposite was synthesized by adding the as-prepared BiOBr and MgFe_2O_4 with 15 wt% loading into 100 mL water containing ZnO and ultrasonicated for 30 minutes. The resulting solution was placed under stirring for 12 hours in room temperature. The precipitates formed were filtered and washed with distilled water for several times. Then, the collected sample was dried in an oven at 80°C for 24 hours and grinded into fine powder using pestle and mortar. Finally, the powder was calcined in a muffle furnace at 450°C for 2 hours. A schematic illustration of the route employed to fabricate $\text{ZnO}/\text{BiOBr}/\text{MgFe}_2\text{O}_4$ is shown in Figure 3.5. The preparation of other photocatalyst combinations: ZnO/BiOBr and $\text{ZnO}/\text{MgFe}_2\text{O}_4$ was conducted using the similar procedure as well.

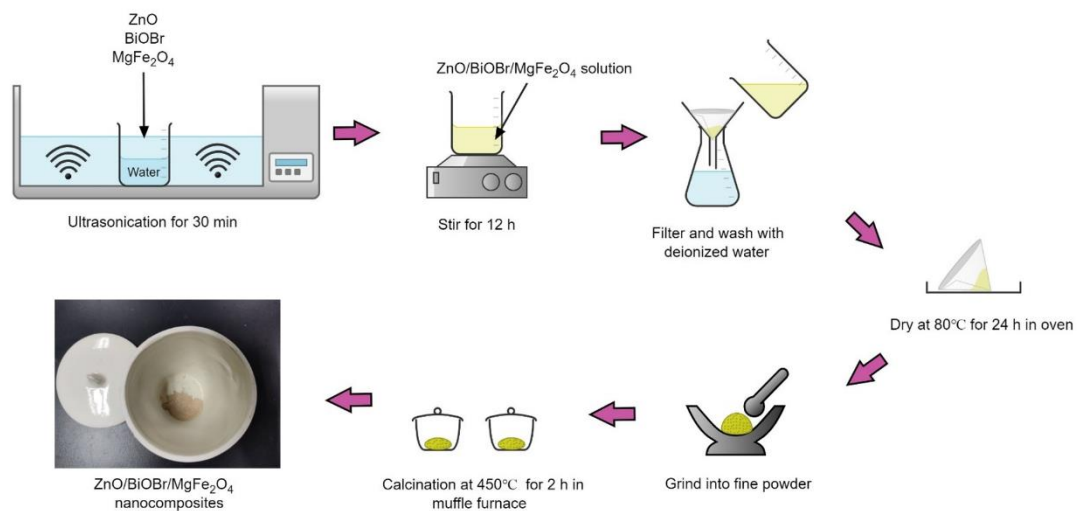


Figure 3.5: Synthesis process of ZnO/BiOBr/MgFe₂O₄ nanocomposites

3.4 Characterization

3.4.1 X-ray Diffraction (XRD)

The crystallographic structure of as-synthesized photocatalysts was determined using Smimadzu XRD-6000 machine at Faculty of Science, UTAR Kampar. The XRD data were scanned at 2θ ranged from 10° to 90° .

3.4.2 Field Emission Scanning Electron Microscopy (FESEM) and Energy Dispersive X-ray (EDX) Spectroscopy

The surface morphology and elemental composition of as-synthesized photocatalysts were examined at Faculty of Science, UTAR Kampar by using an Oxford Instrument X-Max EDS system equipped with a FESEM model of Quanta FEG 450 from the United Kingdom. The analysis was conducted by uniformly distributing the photocatalyst powder on a double-sided carbon adhesive tape attached to aluminium sample stub.

3.4.3 Ultraviolet-Visible Diffuse Reflectance Spectroscopy (UV-vis DRS)

The optical properties as well as band gap energy of as-synthesized photocatalyst samples were investigated using JASCO V-730 UV-vis spectrophotometer, which is accessible at Faculty of Engineering and Green Technology, UTAR Kampar.

3.4.4 Fourier Transform Infrared Spectroscopy-Attenuated Total Reflectance (FTIR-ATR)

FTIR-ATR analysis was performed to analyse the functional group existing in the as-synthesized photocatalyst. The FTIR-ATR data were scanned over the wavelengths ranging from 4000 cm^{-1} to 400 cm^{-1} . This analysis was carried out at Faculty of Science, UTAR Kampar.

3.5 Photocatalytic Activity

The photodegradation of RhB in both aqueous solution and greywater over the as-synthesized powder was performed in a batch reaction system under sunlight irradiation. For photodegradation of RhB in aqueous solution, 0.1 g of catalyst was dispersed in 100 mL RhB solution of 20 ppm and being stirred for 1 hour under dark condition to reach adsorption-desorption equilibrium. The concentration of RhB after equilibration was analysed using JASCO V-730 UV-vis spectrophotometer and recorded as the initial concentration (C_o). Subsequently, the suspension was subjected to constant stirring under sunlight irradiation for 2 hours to initiate the photocatalytic reaction, which is as depicted in Figure 3.6. Then, periodical sampling (4 mL) was conducted from the suspension at every 20 minutes for measurement of RhB concentration (C_t) using the calibration curve of absorbance versus concentration (Figure 3.7).



Figure 3.6: Experimental Setup for Photodegradation of Rhodamine B in aqueous solution

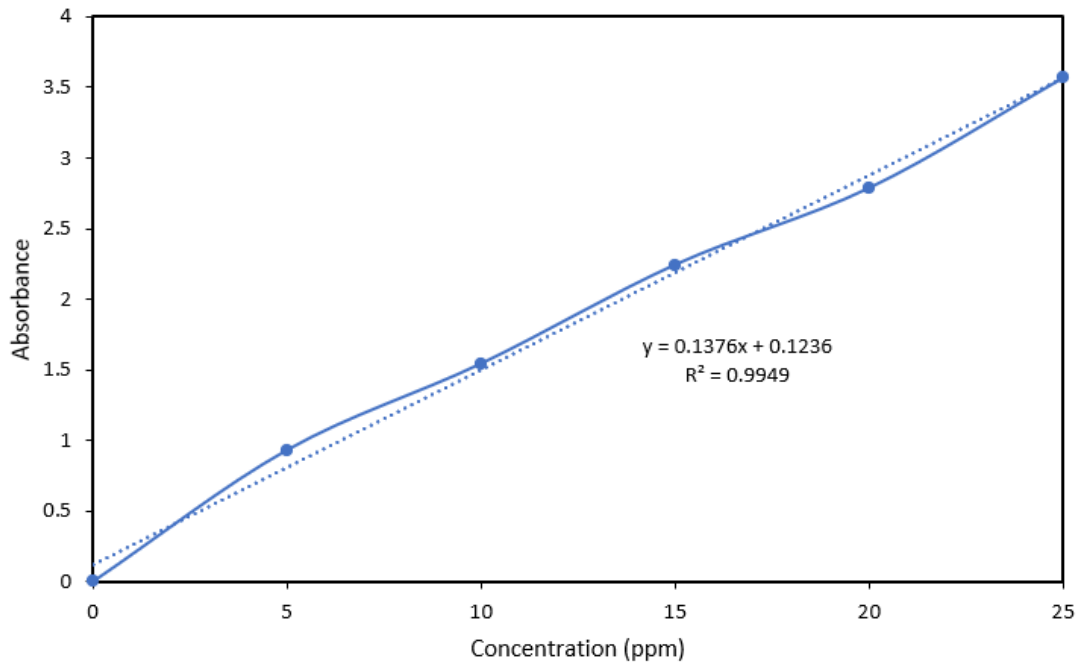


Figure 3.7: Calibration curve of absorbance against RhB concentration

The degradation efficiency was determined using Eq. (3.1):

$$(\%) \text{ degradation} = \frac{(C_o - C_t)}{C_o} \times 100\% \quad (3.1)$$

where C_o and C_t are the equilibrium and concentration at time t for the RhB solution, respectively. Then, the apparent reaction constant, k_{app} was determined by fitting the obtained experimental data into a Langmuir Hinshelwood kinetic model as shown in Eq. (3.2).

$$-\ln \frac{C_t}{C_o} = k_{app}t \quad (3.2)$$

The same experimental procedure was repeated for photodegradation of RhB in greywater, where the suspension was prepared by adding 0.1 g photocatalyst into 100 mL greywater with 20 ppm RhB.

3.6 Phytotoxicity Test

Phytotoxicity evaluation was conducted for the photocatalytically treated RhB-greywater solution using the commercially available mung bean seeds as phytotoxicity assessment indicator. Initially, the surface of green bean seeds was sterilized with acetic acid and rinsed with distilled water for several times. The sterilized seeds were then placed in three petri dishes containing cotton wool wetted by distilled water (control) and RhB-greywater solution (untreated and treated). The seed growth was subsequently monitored for 7 consecutive days. After 7 days, the germinated seeds were removed from the petri dishes and the radicle lengths were measured. The phytotoxicities of each sample was calculated according to Eq. (3.3).

$$(\%) \text{ phytotoxicity} = \frac{\text{radicle length of control} - \text{radicle length of sample}}{\text{radicle length of control}} \times 100 \quad (3.3)$$

CHAPTER 4

RESULT AND DISCUSSION

4.1 Characterization

A wide range of analytical techniques had been employed to characterize the physical, chemical and optical properties of the photocatalysts prepared as powder form. The analytical techniques include Field Emission Scanning Electron Microscopy (FESEM), Energy Dispersive X-ray (EDX), X-ray Diffraction (XRD), Fourier Transform Infrared Spectroscopy-Attenuated Total Reflectance (FTIR-ATR) and Ultraviolet-visible Diffuse Reflectance Spectroscopy (UV-vis DRS).

4.1.1 Field Emission Scanning Electron Microscopy (FESEM)

The morphological structure of the as-synthesized samples was investigated using FESEM. As observed in Figure 4.1 (a), the pristine ZnO exhibited nanoparticle morphology with particle sizes ranging from $0.6 \pm 0.5\mu\text{m}$. Figure 4.1 (b) depicts the FESEM image of bare BiOBr, demonstrating the typical sheet-like morphology that consists of stacked two-dimensional (2D) curved nanosheets with $2.0 \pm 1.5\mu\text{m}$ in diameter. The surface morphology of MgFe_2O_4 is illustrated in Figure 4.1 (c), revealing a spinel structure with irregular coral-shaped rods (length of $2.5 \pm 2\mu\text{m}$). On the other hand, the ZnO/BiOBr/ MgFe_2O_4 nanocomposite was composed of the ZnO nanoparticles, BiOBr nanosheets and MgFe_2O_4 nanorods, which were homogeneously attaching to each other as depicted in Figure 4.1 (d). The obtained FESEM results have denoted the successful incorporation of the single components in constructing a ternary heterostructure.

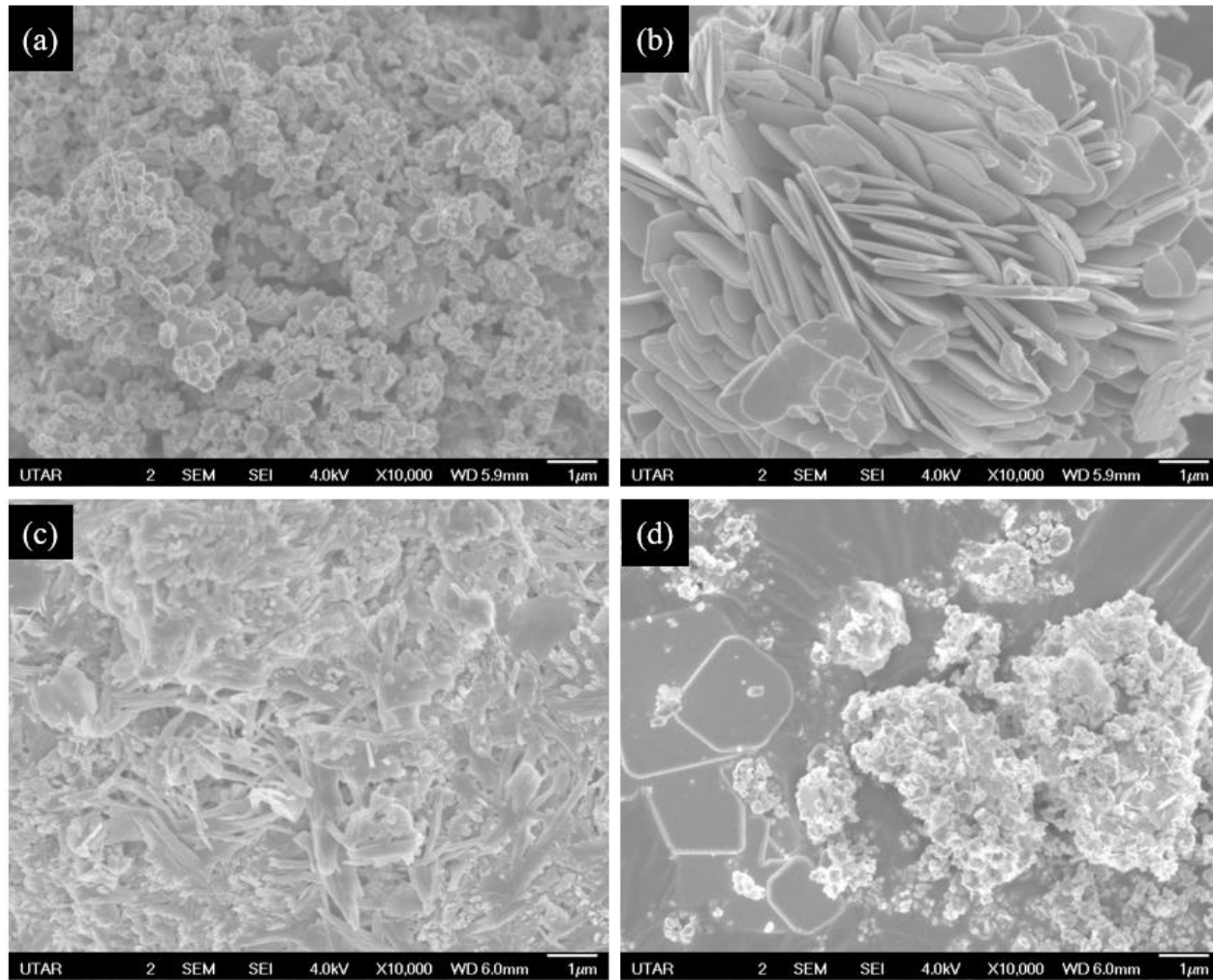


Figure 4.1: FESEM images obtained for (a) ZnO; (b) BiOBr; (c) MgFe₂O₄ and (d) ZnO/BiOBr/MgFe₂O₄.

4.1.2 Energy Dispersive X-ray (EDX)

The elemental composition of the prepared ZnO/BiOBr/MgFe₂O₄ was scrutinized using EDX spectroscopy. Figure 4.2 illustrates the EDX spectra and elemental dot mapping images of ternary ZnO/BiOBr/MgFe₂O₄ nanocomposites. The simultaneous existence of O, Mg, Fe, Zn, Bi and Br elemental peaks as well as nonappearance of impurity peaks in the EDX spectra provided solid evidence to validate the successful synthesis of the ternary nanocomposites. Importantly, as depicted in the EDX mapping images, it should be noted that the elements were well-dispersed throughout the composition, which could impart better photocatalytic efficiency. Furthermore, the percentage weight ratio of elements in the composite is shown in the inset table, which is almost consistent with the stoichiometric amounts taken for preparing ZnO/BiOBr/MgFe₂O₄ nanocomposite.

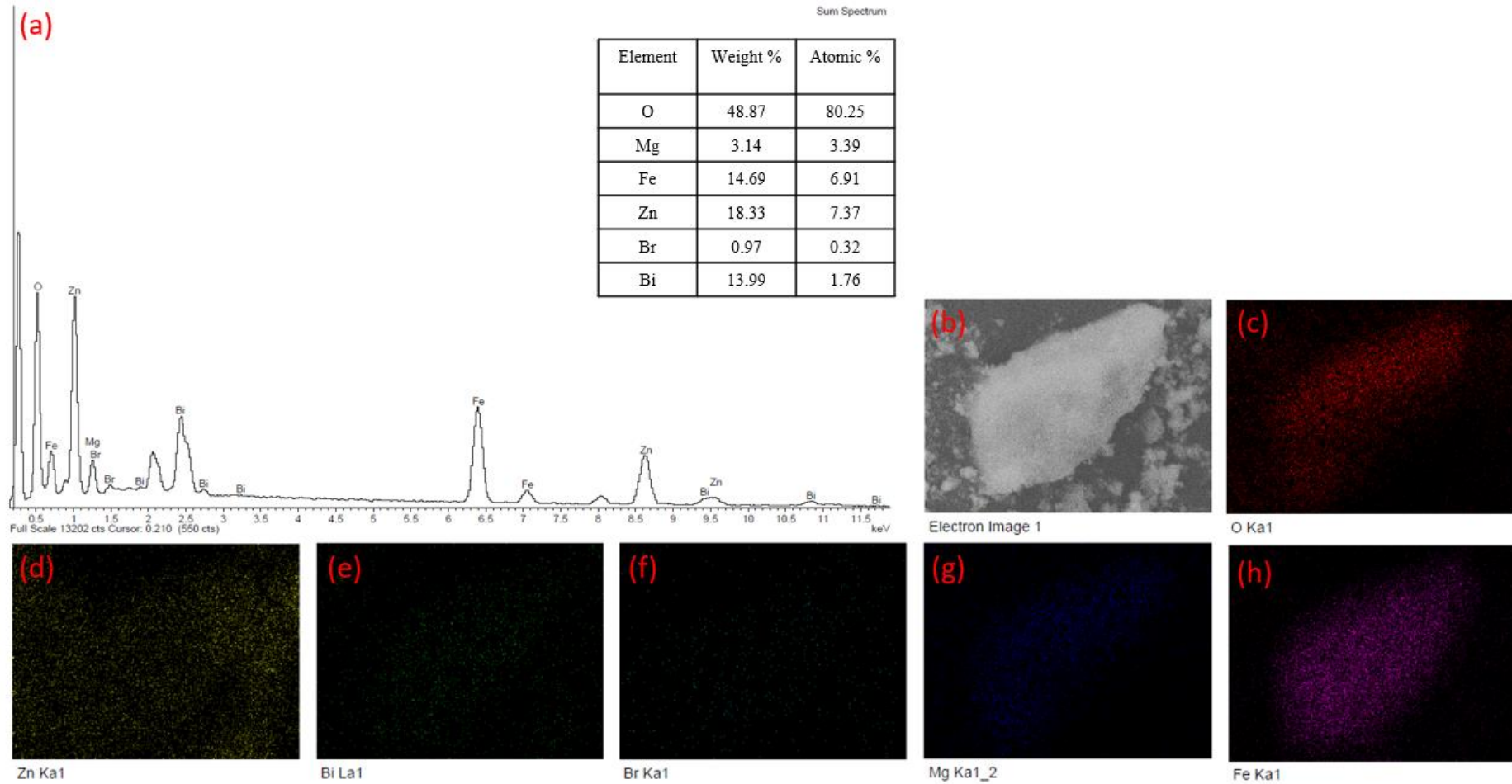


Figure 4.2: (a) The EDX spectra of ZnO/BiOBr/MgFe₂O₄; (b)-(h) elemental dot mapping of ZnO/BiOBr/MgFe₂O₄.

4.1.3 Fourier Transform Infrared Spectroscopy-Attenuated Total Reflectance (FTIR-ATR)

FTIR-ATR was performed to determine the functional group of the as-synthesized samples. Figure 4.3 depicts the FTIR-ATR spectra of ZnO, BiOBr, MgFe₂O₄ and ZnO/BiOBr/MgFe₂O₄. In ZnO, the sharp absorption peak at 499 cm⁻¹ is ascribed to the Zn-O stretching vibration in tetrahedral coordination (Janani et al., 2022). Apart from Zn-O, all additional bands that may form as a result of adsorbed species applied during synthesis process are absent owing to high temperature calcinations, which is consistent with the findings by Imran et al (Imran et al., 2017). Meanwhile, the two characteristics peaks of BiOBr at 508 cm⁻¹ and 1382 cm⁻¹ are assigned to the symmetric Bi-O stretching vibration and the antisymmetric Bi-Br stretching vibration, respectively (Qin et al., 2022). For MgFe₂O₄, the absorption bands observed at 1394, 1432, 1648 and 3369 cm⁻¹ correspond to the stretching and bending of O-H group of water (Israr et al., 2020; Syed et al., 2021). On the other hand, the prominent peaks of the typical spinel ferrites are also revealed at 553 cm⁻¹ and 863 cm⁻¹, indicating the existence of tetrahedral M-O bond and octahedral M-O bond, respectively (Fardood et al., 2022). In the case of ZnO/BiOBr/MgFe₂O₄ composite, the FTIR-ATR spectrum exhibits the similar characteristic peaks with those of ZnO, BiOBr and MgFe₂O₄, with the overlapping of peaks between ZnO and BiOBr observed at 501 cm⁻¹ and occurrence of spinel ferrite characteristic peak at 875 cm⁻¹ due to the MgFe₂O₄ deposition, suggesting that these elements were the key components of the composite.

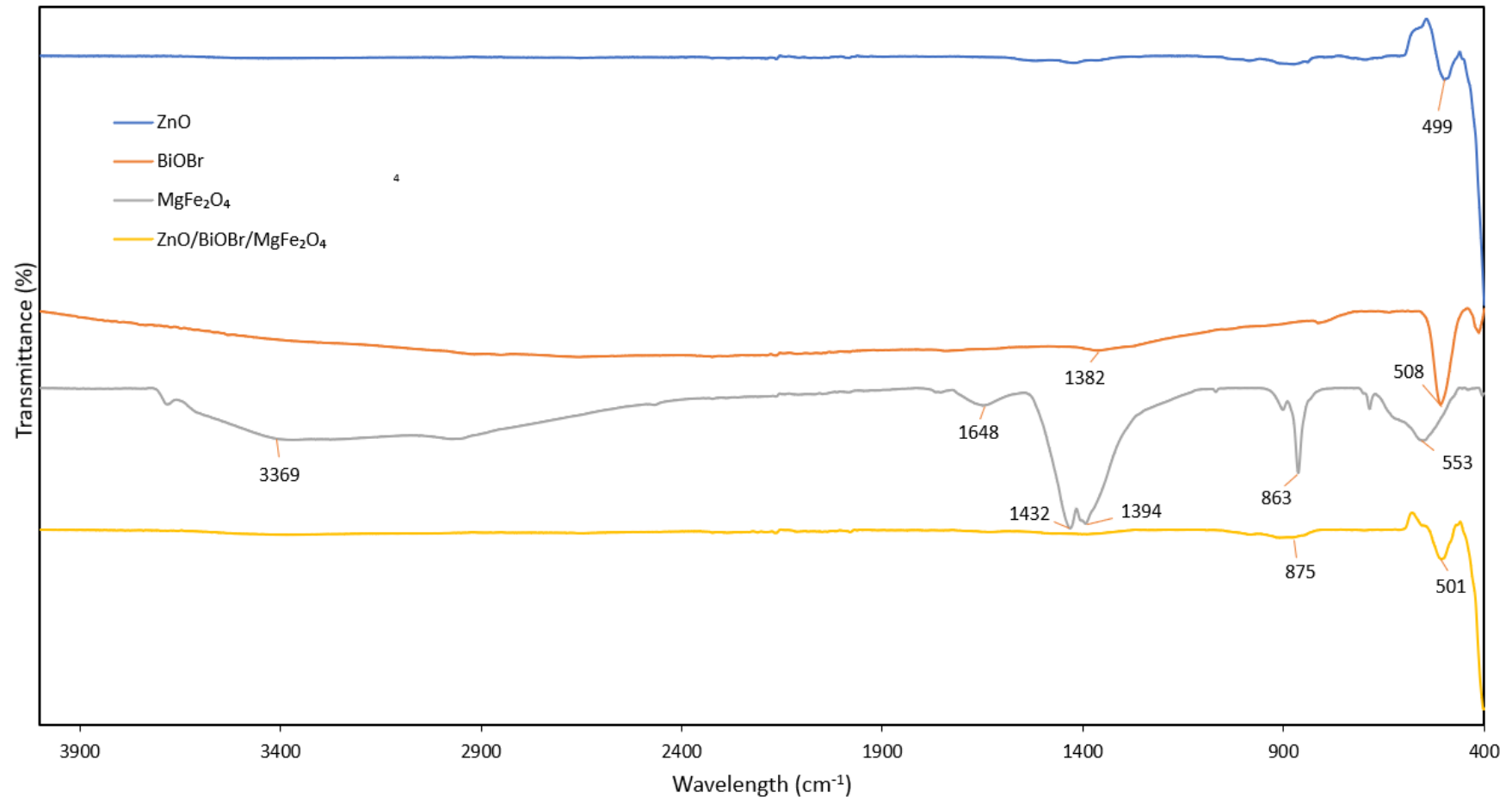


Figure 4.3: FTIR-ATR spectra of ZnO, BiOBr, MgFe₂O₄ and ZnO/BiOBr/MgFe₂O₄.

4.1.4 Ultraviolet-Visible Diffuse Reflectance Spectroscopy (UV-vis DRS)

The UV-vis spectroscopy in diffuse reflectance mode has also been employed to all prepared samples to study the optical properties of synthesized nanostructures. The acquired spectral patterns and corresponding band gap energies (E_g) are demonstrated in Figure 4.4 and 4.5. The occurrence of absorption edges is attributed to the charge transportation between valence band and conduction band. It is clearly observed that the pristine ZnO shows an absorption peak (381 cm^{-1}) in the UV region, implying its photoactivation upon UV irradiation. In a stark contrast, pure BiOBr and MgFe₂O₄ both exhibits good photosensitivity at the absorption band-edge of the visible light range. Despite the absence of absorption peak in the visible light spectrum for ZnO/BiOBr/MgFe₂O₄, the introduction of BiOBr and MgFe₂O₄ had led to an increased absorption intensity in the visible region, offering more probabilities for enhancing photocatalytic performance. According to the Tauc plot, the band gap values for ZnO, BiOBr, MgFe₂O₄ and ZnO/BiOBr/MgFe₂O₄ are estimated to be 3.31, 2.85, 1.97 and 3.26 eV, respectively. As compared to the pristine ZnO, the ternary composite ZnO/BiOBr/MgFe₂O₄ has a lower band gap value plausibly due to the incorporation of BiOBr and MgFe₂O₄ with narrow band gaps, which offers more stimulation of photogenerated electron-hole pairs and improve the light utilization efficiency thereby leading to escalated photocatalytic activity.

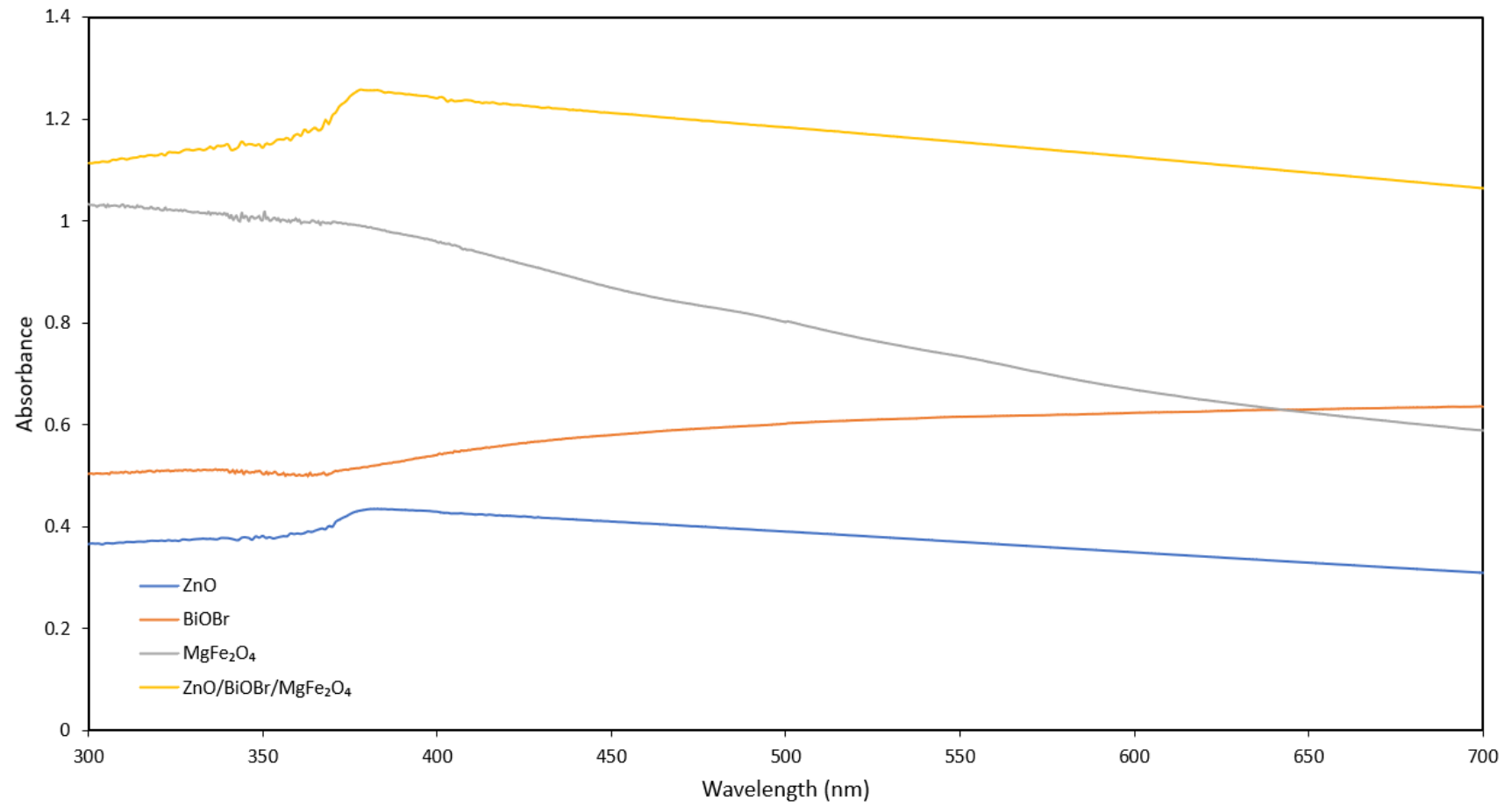


Figure 4.4: UV-vis diffuse reflectance spectra of ZnO, BiOBr, MgFe₂O₄ and ZnO/BiOBr/MgFe₂O₄.

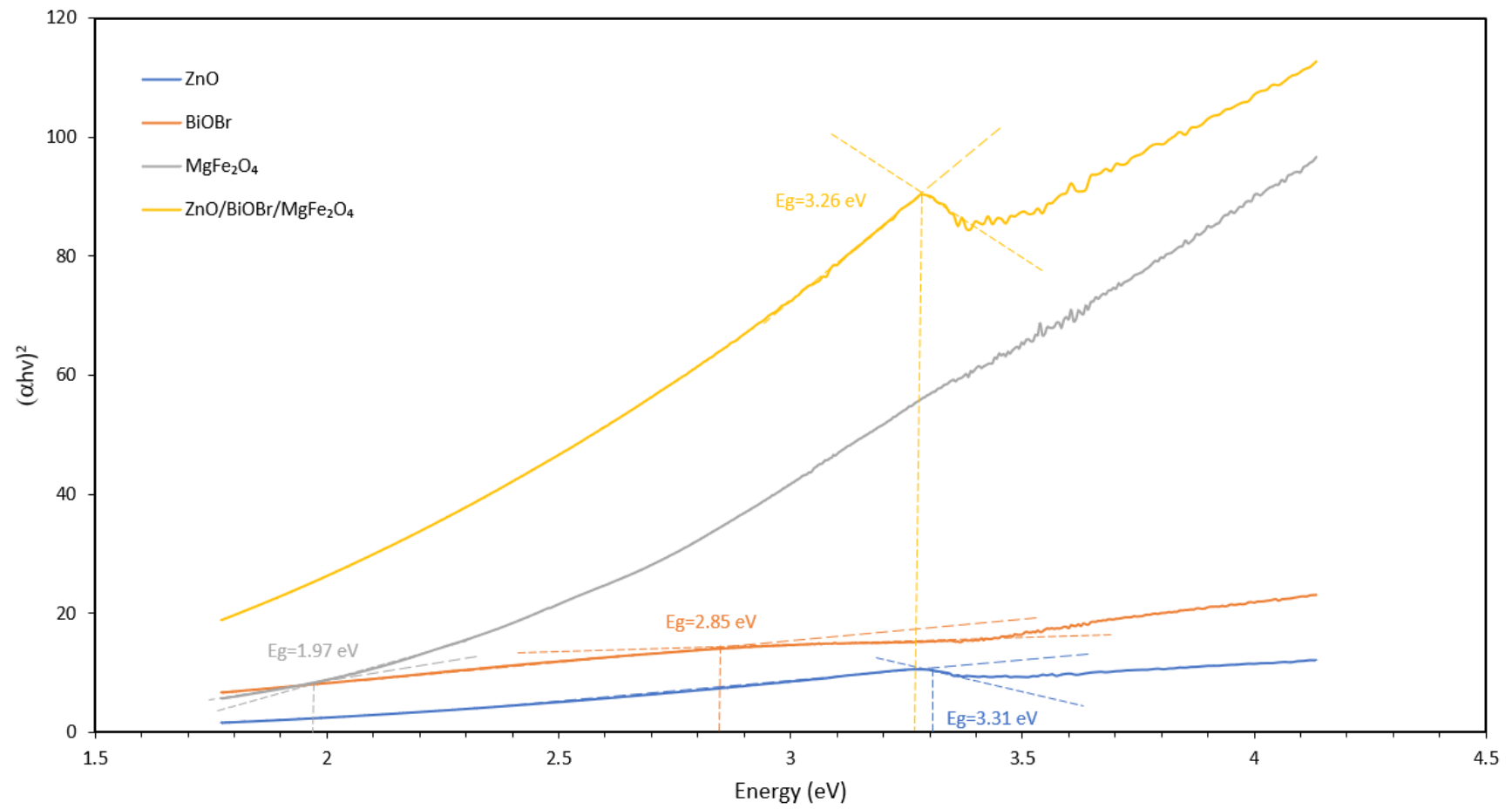


Figure 4.5: Energy gap analysis of ZnO, BiOBr, MgFe₂O₄ and ZnO/BiOBr/MgFe₂O₄ via Tauc plot.

4.1.5 X-Ray Diffraction (XRD)

XRD analysis was applied to elucidate the crystallinity of the as-synthesized samples and the diffraction patterns are shown in Figure 4.6. As depicted in Figure 4.6 (a), the intense peaks located at 31.84° , 34.52° , 36.32° , 47.68° , 56.66° , 62.94° and 68.1° can be assigned to (100), (002), (101), (102), (110), (103) and (112) crystallographic planes of the hexagonal wurtzite ZnO (Kumari et al., 2022). For BiOBr NPs (Figure 4.6 (b)), it displays strong reflections at 10.98° , 21.96° , 25.28° , 31.78° , 33.24° , 40.28° , 44.74° , 50.76° , 69.66° and 78.88° for (001), (002), (101), (102), (110), (112), (200), (104), (220) and (310) planes, respectively, revealing consistent finding with the literature which corresponds to tetragonal matlockite structure of BiOBr (Lyu et al., 2019). The MgFe_2O_4 NPs diffraction peaks are clearly observed in Figure 4.6 (c) with $2\theta = 30.16^\circ$, 34.28° , 38.06° , 44.76° , 48.42° , 62.68° , 65.16° and 78.28° , which are indexed respectively as (220), (311), (222), (400), (331), (440), (531) and (533) planes of MgFe_2O_4 , demonstrating its face-centred cubic structure (Waheed et al., 2022).

On the other hand, as shown in Figure 4.6 (d), the XRD spectra of $\text{ZnO}/\text{BiOBr}/\text{MgFe}_2\text{O}_4$ is composed of sharp and strong diffraction peaks of ZnO, BiOBr and MgFe_2O_4 , with no shifted peaks that would indicate lattice expansion or contraction. The weak peaks of (001), (002), (101), (220), (400), (200) and (533) plane might be attributed to the low dosage of BiOBr and MgFe_2O_4 . Furthermore, no extra diffraction peaks can be identified in the ternary heterostructure, implying the high purity of the sample produced and non-occurrence of ZnO crystal phase transformation following in-situ growth of BiOBr and deposition of MgFe_2O_4 .

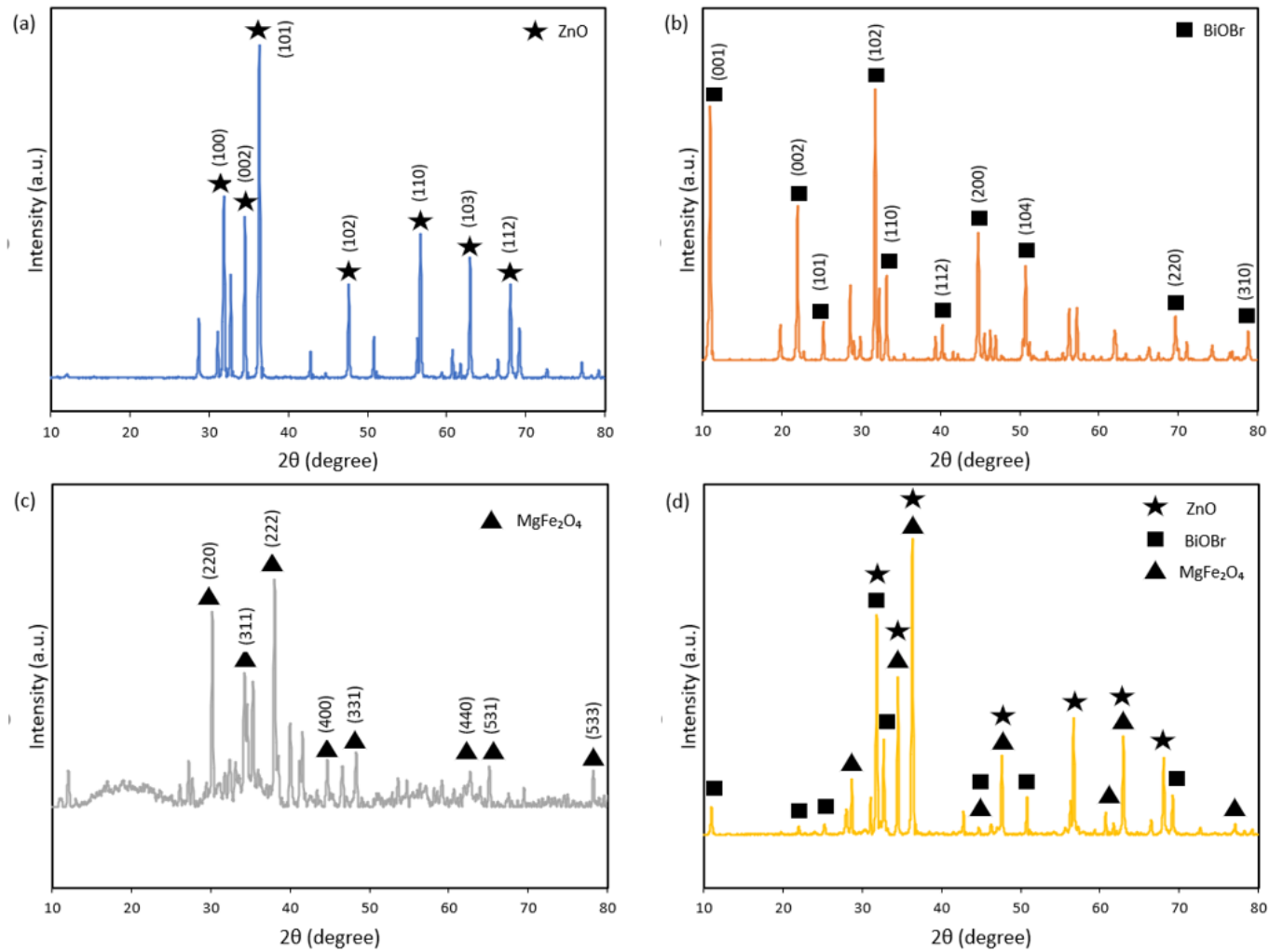


Figure 4.6: XRD spectra of as-obtained photocatalysts: (a) ZnO, (b) BiOBr, (c) MgFe₂O₄ and (d) ZnO/BiOBr/MgFe₂O₄.

4.2 Photocatalytic Degradation Studies

The photocatalytic activity of the prepared samples is assessed by tracking the degradation of RhB in both aqueous solution and greywater under sunlight irradiation. In each experiment, 1 g/L of photocatalysts were dispersed in 20 ppm of RhB solution and subsequently irradiated to sunlight with continuous stirring for 3 hours. Figure 4.7 (a) and Figure 4.8 (a) reveal that the absorption band intensities of RhB gradually decay over extended period of time in presence of ZnO/BiOBr/MgFe₂O₄ ternary composite, with absorption peaks located at 550 nm. The experimental results depicted in Figure 4.7 (b) and Figure 4.8 (b) corroborated that the natural photolysis of RhB under sunlight irradiation was negligible, and there was no substantial degradation of the RhB in the presence of photocatalysts under dark circumstances, implying that the RhB degradation is primarily induced by the photocatalytic activity of excited semiconductors. The photodegradation efficiencies of RhB for ZnO, BiOBr, MgFe₂O₄, ZnO/BiOBr, ZnO/MgFe₂O₄ and ZnO/BiOBr/MgFe₂O₄ are found to be 90.42%, 92.06%, 8.80%, 91.42%, 88.02% and 96.14% in aqueous solution, and 80.80%, 90.03%, 3.62%, 88.25%, 85.07% and 93.59% in greywater, respectively. It can be observed that the ZnO/BiOBr/MgFe₂O₄ ternary heterojunction system exhibited better photocatalytic performance for degradation of RhB in both aqueous solution and greywater as compared to pristine single and binary photocatalysts. Interestingly, the photocatalytic efficiency of ZnO/BiOBr/MgFe₂O₄ in greywater decreased unremarkably by 2.55% as compared with the degradation of RhB in aqueous solution, which could be ascribed to the existence of other pollutants in greywater effluent that vigorously competes for the active reaction sites on the heterostructure surface (Chong et al., 2015).

Subsequently, the kinetics of RhB degradation in aqueous solution and greywater was studied by fitting to a Langmuir Hinshelwood kinetic model and corresponding results are summarized in Figure 4.7 (c) and Figure 4.8 (c). The plots of $-\ln(C/C_0)$ versus irradiation time (t) were unveiled to be linear correlation, indicating that the reaction conforms to the pseudo-first-order kinetics. The photodegradation rate constant (k_{app}) values of RhB dye in aqueous solution for ZnO, BiOBr, MgFe₂O₄, ZnO/ BiOBr, ZnO/MgFe₂O₄ and ZnO/BiOBr/MgFe₂O₄ are estimated as 0.0102, 0.0132, 0.004, 0.0106, 0.0110 and 0.0153 respectively, while those of the RhB in greywater are 0.0088, 0.0112, 0.0003, 0.01, 0.0096 and 0.0117, respectively. For ZnO/BiOBr/MgFe₂O₄ ternary nanocomposite, the $k_{app} \sim 0.0153$ for aqueous solution

and $k_{app} \sim 0.0117$ for greywater, as shown in Figure 4.7 (d) and Figure 4.8 (d), are the highest among all the photocatalysts, which is 1.5- and 1.33-fold higher than the pristine ZnO in both the respective cases. This phenomenon could be attributed to the synergistic effect from the coupling of BiOBr and MgFe₂O₄, which imparts elevated light absorption and further enhances the separation and migration efficiency of photo-generated electron-hole pairs, as confirmed by UV-Vis diffuse absorption spectra spectroscopy.

Previous studies conducted by Gao et al. (2022) on ZnO-based ternary composite had reported similar findings whereby they proposed a novel ternary ZnO@ZIF-8/AgI composite for photodegradation of selected tetracycline (TC) upon visible light illumination. The ternary heterostructure was constructed via in-situ seamless growth of zeolitic imidazolate framework-8 (ZIF-8) nanofilms followed by deposition of AgI on ZnO@ZIF-8. Their photodegradation studies reveal that the ZnO@ZIF-8/AgI demonstrated highest photocatalytic activity, which was superior to unitary and binary photocatalysts. The photocatalytic efficiencies of ZnO@ZIF-8 and ZnO@ZIF-8/AgI increased by 34% and 90% compared with the ZnO, respectively, suggesting that the incorporation of ZIF-8 and AgI in constructing a ternary heterostructure can further enhance the photocatalytic potential of ZnO. They inferred that the improved photocatalytic activity of ternary composite may occur due to the (i) large specific surfaces and porosities of ZIF-8 shells which offered a favorable environment for the preconcentration of TC onto the photocatalyst surface, enhancing the utilization efficiency of photogenerated electron-hole pairs, the (ii) efficient photosensitivity towards visible light region and the (iii) increase in the trappings of electron and holes, facilitating the reduction of recombination rate. Another comparable finding was proclaimed by Nguyen et al. (2020) on the removal of various dyes over TiO₂/ZnO/rGO (TZR) composite under UV/simulated solar illumination. The decreasing order of photocatalytic activities for RhB removal is found to be TZR > TiO₂/ZnO > TiO₂ > ZnO, suggesting that TZR composites exhibited the highest photocatalytic performance. They explained by the similar reasoning as the previous study whereby the incorporation of rGO, TiO₂ and ZnO contributed to the narrowing of bandgap energy and increased the light absorption in the visible light region thereby led to improved photocatalytic performance of TZR composite.

Apart of good photocatalytic performance, the good recyclability of photocatalyst is another key aspect to be taken into consideration for practical application. Figure 4.9 illustrates the recycling experiment for ZnO/BiOBr/MgFe₂O₄ ternary composite through magnetic separation. It shows that the as-synthesized ternary photocatalyst can be easily attracted by the magnet owing to the intrinsic magnetic properties offered by MgFe₂O₄ spinel ferrite, which suggests its great potential for practical application.

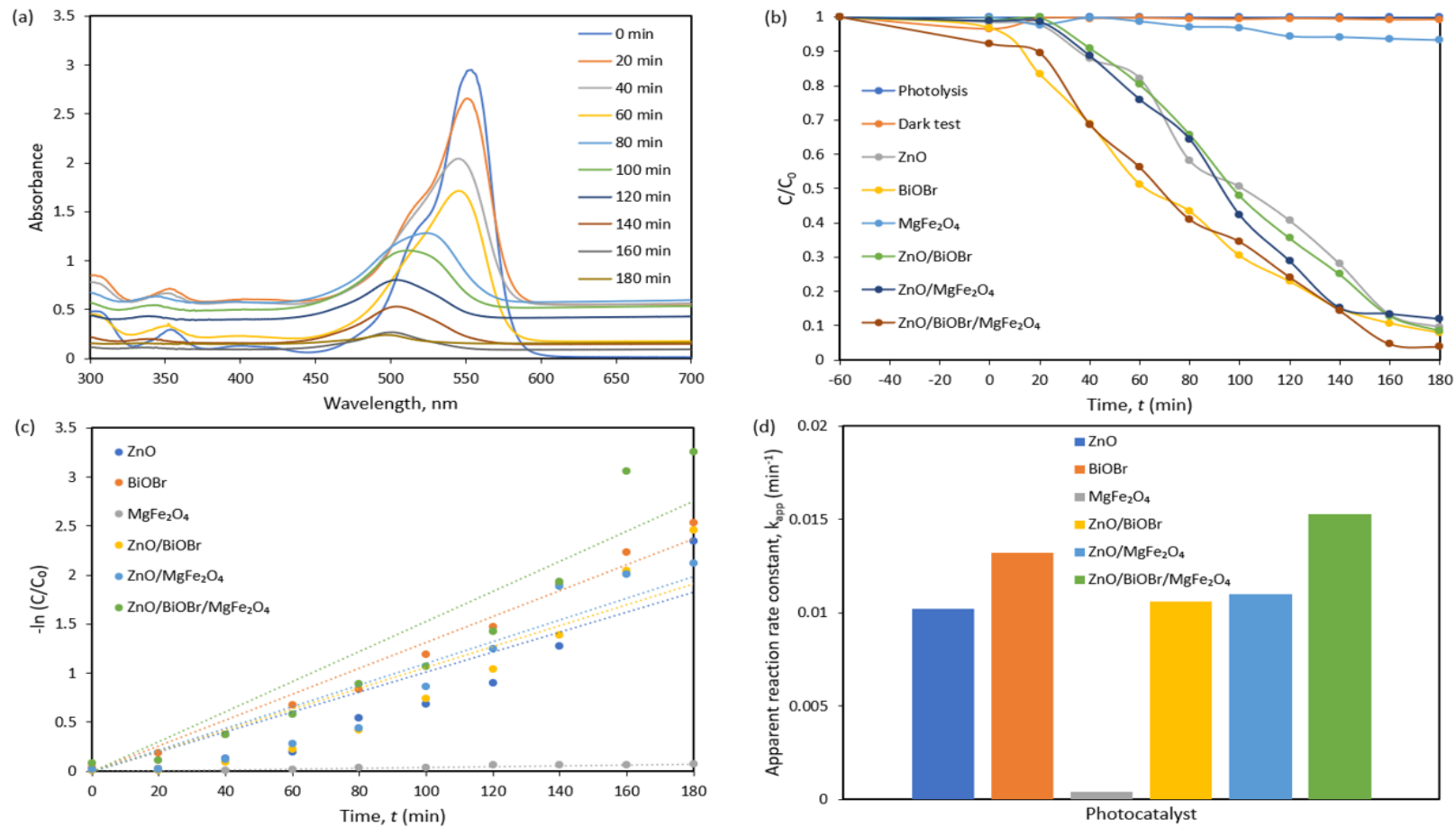


Figure 4.7: Photocatalytic activity of as-prepared samples for RhB degradation in aqueous solution. (a) Absorption spectra of RhB dyes after 180 min of sunlight exposure on ZnO/BiOBr/MgFe₂O₄ ternary composite; (b) profiles of RhB photodegradation; (c) kinetic curves and (d) apparent reaction rate constants (k_{app}) obtained by applying the pseudo-first-order model.

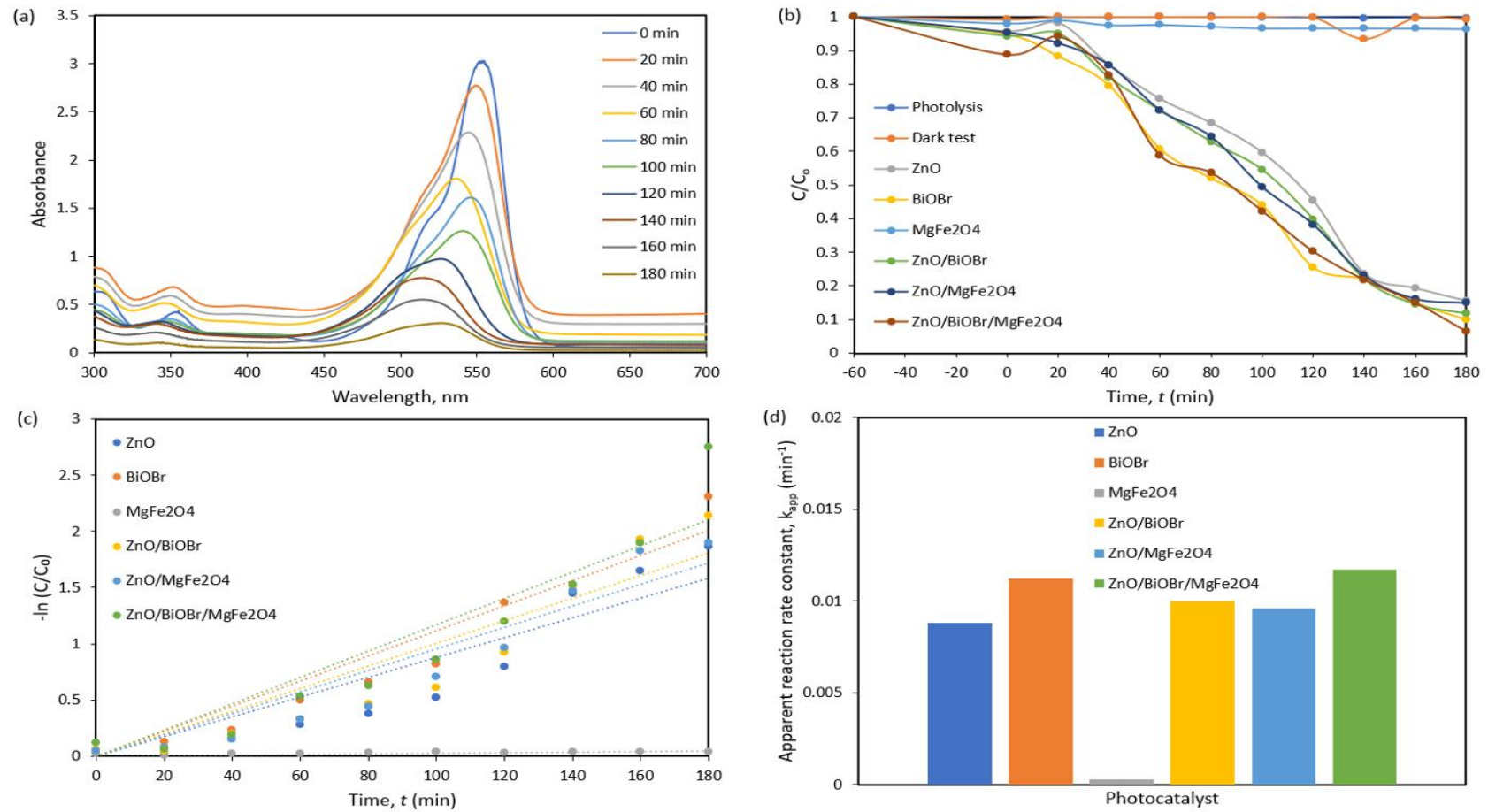


Figure 4.8: Photocatalytic activity of as-prepared samples for RhB degradation in greywater. (a) Absorption spectra of RhB dyes after 180 min of sunlight exposure on ZnO/BiOBr/MgFe₂O₄ ternary composite; (b) profiles of RhB photodegradation; (c) kinetic curves and (d) apparent reaction rate constants (k_{app}) obtained by applying the pseudo-first-order model.



Figure 4.9: Magnetic recovery of $\text{ZnO}/\text{BiOBr}/\text{MgFe}_2\text{O}_4$ ternary composites after photocatalysis.

4.3 Phytotoxicity Evaluation

The direct discharge of harmful organic pollutants, particularly synthetic dyes like RhB might pose a profound impact on the environment and human health, including a direct contamination on aquatic system as well as impedance of soil fertility. Thus, it is substantive and meaningful to evaluate the phytotoxicity of RhB dyes and the treatment effectiveness. A cultivation study of mung bean sprouts was conducted to evaluate the phytotoxicity of RhB dyes before and after the photocatalytic treatment over ZnO/BiOBr/MgFe₂O₄ as shown in Figure 4.10 (a)-(d). After incubation for consecutive 7 days, the radicle length of mung beans irrigated with deionized water (control) was measured to be 2.8 cm. However, the inhibition of radicle growth was observed for the seeds exposed to untreated RhB solution, which showed no germination at all. Impressively, the mung beans in the presence of ZnO/BiOBr/MgFe₂O₄ exhibited significantly higher radicle growth (1.8 cm) after degradation, with only 35% reduction in radicle length as compared to the control.

As shown in Figure 4.10 (a), the phytotoxicities of the RhB dyes was found in order of pure RhB solution before degradation > treated solution > control, with percentages of 100%, 35.71% and 0%, respectively. This suggested that the ZnO/BiOBr/MgFe₂O₄ can degrade the RhB dyes and reduce the toxicity of treated water in an impressive manner, which provide new insights on the safety release of RhB dyes during treatment process. These outcomes were highly consistent with the previous study done by Venkatesh and Sakthivel, whereby they also performed a phytotoxicity test on methylene blue (MB) dyes using *Vigna Radiata* as assessment indicator (Venkatesh and Sakthivel, 2022). They discovered a noteworthy degree of inhibition up to 40% on the germination rate of seedlings irrigated with untreated MB dyes, which is on contrary to the 71.10% seed germination index for the MB solution degraded over the Zn doped SnO₂ photocatalyst, indicating a substantial reduction in phytotoxicity of dye effluent after photodegradation.

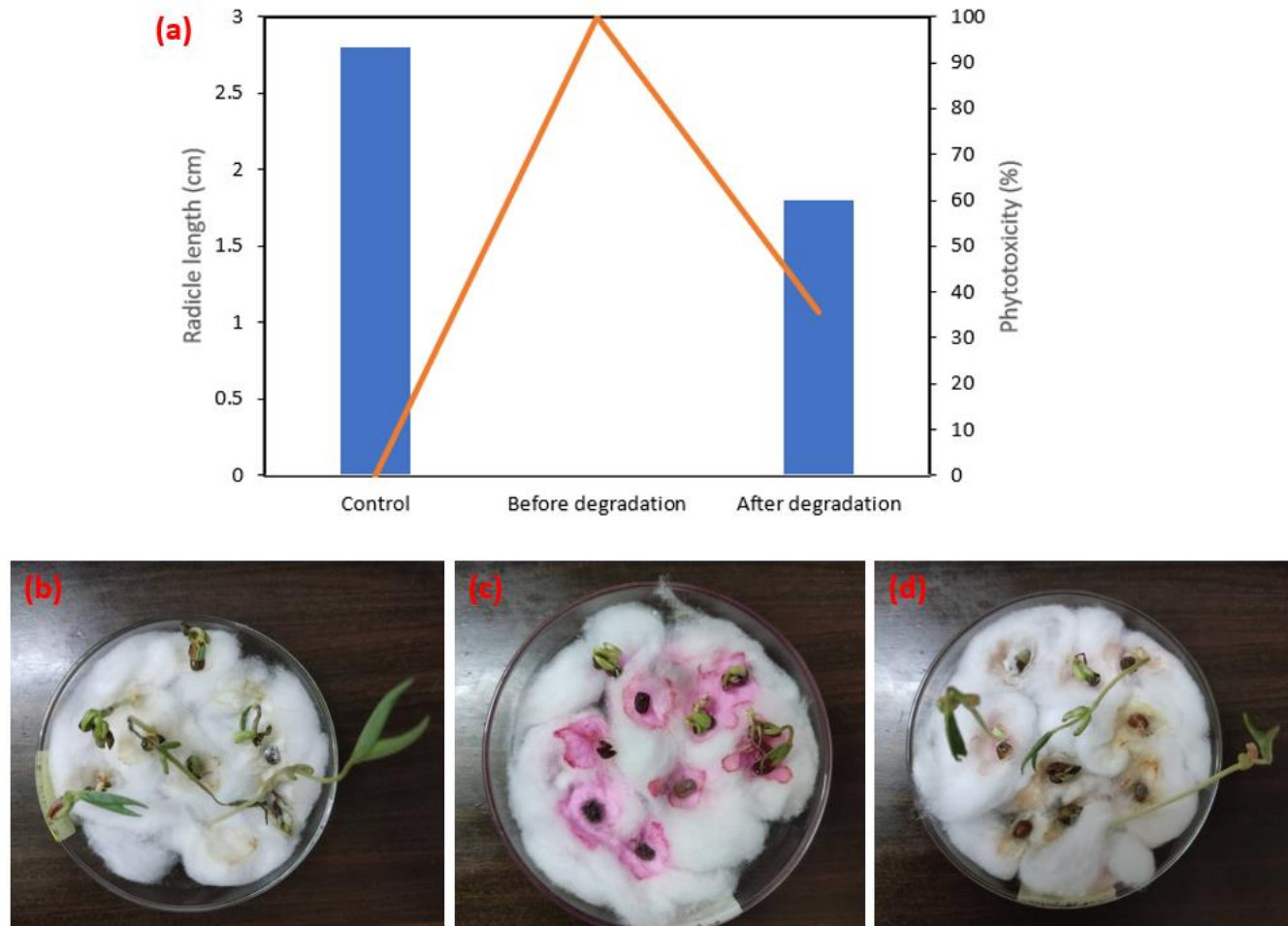


Figure 4.10: (a) Phytotoxicity of RhB dye in greywater before and after degradation using ZnO/BiOBr/MgFe₂O₄; (b) control; (c) before degradation and (d) after degradation after 7 days.

CHAPTER 5

CONCLUSION AND RECOMMENDATION

5.1 Conclusion

In summary, a magnetically separable novel ternary ZnO/BiOBr/MgFe₂O₄ photocatalyst was successfully developed via a low cost ultrasonic-deposition method for degradation of RhB dyes in aqueous solution and greywater under sunlight irradiation. The as-synthesized samples were characterized by various characterization techniques including FESEM, EDX, FTIR-ATR, UV-vis DRS and XRD to examine their physiochemical and optical properties. FESEM images showed the homogeneous attachment of ZnO nanoparticles and deposition of MgFe₂O₄ nanorods over the 2D curved BiOBr nanosheets towards the construction of ternary heterostructure. Furthermore, EDX results revealed the uniform distribution of O, Mg, Fe, Zn, Bi and Br in ZnO/BiOBr/MgFe₂O₄ ternary composite with no other characteristic peaks being observed, implying the high purity of as-obtained photocatalyst. Moreover, FTIR-ATR spectra confirmed the existence of characteristic peaks of ZnO, BiOBr and MgFe₂O₄ in the prepared ZnO/BiOBr/MgFe₂O₄ sample. The improved light absorption of the ternary composite was also validated from the increased intensity of visible light absorption in UV-vis DRS spectra as well as the narrowing of band gap in Tauc plot. In addition, the diffraction patterns in XRD spectra of ternary composite were composed of the distinguishing peaks of corresponding pristine components, suggesting the good purity and crystallinity of the fabricated ternary heterostructure. In photoactivity test, as compared to the other photocatalysts, the ZnO/BiOBr/MgFe₂O₄ ternary composite exhibited much better photocatalytic performance for degradation of RhB dyes in both aqueous solution and greywater upon sunlight illumination, with degradation efficiencies up to 96.14% and 93.59%, respectively. It is also noteworthy to mention that the ZnO/BiOBr/MgFe₂O₄ ternary photocatalyst can be easily recycled from the treated solution using an external magnet for industrial application. Lastly, the

phytotoxicity studies demonstrated 64.29% reduction in phytotoxicity for the RhB solution after degradation as compared to the untreated raw RhB solution.

5.2 Recommendation

Upon completion of this project, a few recommendations can be implemented in further photocatalytic studies:

- a) The effect of other parameters affecting photocatalytic activity such as initial dye concentration, pH, light intensity, catalyst loading and presence of oxidizing agent should be scrutinized to acquire in-depth understanding on the photocatalytic ability of ZnO/BiOBr/MgFe₂O₄.
- b) Scavenger test should be conducted to explore the roles of each reacting species in RhB degradation.
- c) Reusability test should be conducted to assess the stability and efficiency of the used ZnO/BiOBr/MgFe₂O₄ ternary composite.
- d) The photodegradation mechanism of RhB should be studied using High Performance Liquid Chromatography (HPLC) and Gas Chromatography (GC).

REFERENCES

- Albiss, B. and Abu-Dalo, M., 2021. Photocatalytic Degradation of Methylene Blue Using Zinc Oxide Nanorods Grown on Activated Carbon Fibers. *Sustainability*, 13(9), p.4729.
- Al-Kahtani, A., 2017. Photocatalytic Degradation of Rhodamine B Dye in Wastewater Using Gelatin/CuS/PVA Nanocomposites under Solar Light Irradiation. *Journal of Biomaterials and Nanobiotechnology*, 8, pp.66-82.
- Allé, P., Fanou, G., Robert, D., Adouby, K. and Drogui, P., 2020. Photocatalytic degradation of Rhodamine B dye with TiO₂ immobilized on SiC foam using full factorial design. *Applied Water Science*, 10(9).
- Agrawal, K. and Verma, P., 2020. Myco-valorization approach using entrapped *Myrothecium verrucaria* ITCC-8447 on synthetic and natural support via column bioreactor for the detoxification and degradation of anthraquinone dyes. *International Biodeterioration & Biodegradation*, 153, p.105052.
- Ahmed, S. and Haider, W., 2018. Heterogeneous photocatalysis and its potential applications in water and wastewater treatment: a review. *Nanotechnology*, 29(34), p.342001.
- Avlonitis, S., Poullos, I., Sotiriou, D., Pappas, M. and Moutesidis, K., 2008. Simulated cotton dye effluents treatment and reuse by nanofiltration. *Desalination*, 221(1-3), pp.259-267.
- Baldev, E., MubarakAli, D., Ilavarasi, A., Pandiaraj, D., Ishack, K. and Thajuddin, N., 2013. Degradation of synthetic dye, Rhodamine B to environmentally non-toxic products using microalgae. *Colloids and Surfaces B: Biointerfaces*, 105, pp.207-214.
- Bai, L., Huang, H., Yu, S., Zhang, D., Huang, H. and Zhang, Y., 2021. Role of transition metal oxides in g-C₃N₄-based heterojunctions for photocatalysis and supercapacitors. *Journal of Energy Chemistry*, 64, pp.214-235.
- Battula, H., Bommi, S., Bobde, Y., Patel, T., Ghosh, B. and Jayanty, S., 2021. Distinct rhodamine B derivatives exhibiting dual effect of anticancer activity and fluorescence property. *Journal of Photochemistry and Photobiology*, 6, p.100026.
- Blok, C., De Kreijl, C., Baas, R. and Wever, G., 2008. ANALYTICAL METHODS USED IN SOILLESS CULTIVATION. *Soilless Culture*, pp.245-289.

- Boukos, N., Chandrinou, C. and Travlos, A., 2012. Zinc vacancies and interstitials in ZnO nanorods. *Thin Solid Films*, 520(14), pp.4654-4657.
- Byrne, J., Dunlop, P., Hamilton, J., Fernández-Ibáñez, P., Polo-López, I., Sharma, P. and Vennard, A., 2015. A Review of Heterogeneous Photocatalysis for Water and Surface Disinfection. *Molecules*, 20(4), pp.5574-5615.
- Chaplin, M., 2001. Water: its importance to life. *Biochemistry and Molecular Biology Education*, 29(2), pp.54-59.
- Chong, M., Cho, Y., Poh, P. and Jin, B., 2015. Evaluation of Titanium dioxide photocatalytic technology for the treatment of reactive Black 5 dye in synthetic and real greywater effluents. *Journal of Cleaner Production*, 89, pp.196-202.
- Christy, E., Amalraj, A., Rajeswari, A. and Pius, A., 2021. Enhanced photocatalytic performance of Zr(IV) doped ZnO nanocomposite for the degradation efficiency of different azo dyes. *Environmental Chemistry and Ecotoxicology*, 3, pp.31-41.
- Dai, R., Zhang, L., Ning, J., Wang, W., Wu, Q., Yang, J., Zhang, F. and Wang, J., 2021. New insights into tuning BiOBr photocatalysis efficiency under visible-light for degradation of broad-spectrum antibiotics: Synergistic calcination and doping. *Journal of Alloys and Compounds*, 887, p.161481.
- Dao, T., Ha, T., Nguyen, T., Le, H., Ha-Thuc, C., Nguyen, T., Perre, P. and Nguyen, D., 2021. Effectiveness of photocatalysis of MMT-supported TiO₂ and TiO₂ nanotubes for rhodamine B degradation. *Chemosphere*, 280, p.130802.
- Das, A., Patra, M., Kumar P, M., Bhagavathiachari, M. and Nair, R., 2021. Role of type II heterojunction in ZnO–In₂O₃ nanodiscs for enhanced visible-light photocatalysis through the synergy of effective charge carrier separation and charge transport. *Materials Chemistry and Physics*, 263, p.124431.
- Department of Environment, 2021. [online] Doe.gov.my. Available at: <https://www.doe.gov.my/portalv1/wp-content/uploads/2015/01/Environmental_Quality_Industrial_Effluent_Regulations_2009_-_P.U.A_434-2009.pdf> [Accessed 13 August 2021].

- Dey, S., Das, S. and Kar, A., 2021. Role of precursor dependent nanostructures of ZnO on its optical and photocatalytic activity and influence of FRET between ZnO and methylene blue dye on photocatalysis. *Materials Chemistry and Physics*, 270, p.124872.
- Długosz, O., Szostak, K. and Banach, M., 2019. Photocatalytic properties of zirconium oxide–zinc oxide nanoparticles synthesised using microwave irradiation. *Applied Nanoscience*, 10(3), pp.941-954.
- Doan, T., Minh Chu, T., Dinh, T., Nguyen, T., Tu Vo, T., Nguyen, N., Nguyen, B., Nguyen, T. and Pham, T., 2020. Adsorptive Removal of Rhodamine B Using Novel Adsorbent-Based Surfactant-Modified Alpha Alumina Nanoparticles. *Journal of Analytical Methods in Chemistry*, 2020, pp.1-8.
- Elghniji, K., Hentati, O., Mlaik, N., Mahfoudh, A. and Ksibi, M., 2012. Photocatalytic degradation of 4-chlorophenol under P-modified TiO₂/UV system: Kinetics, intermediates, phytotoxicity and acute toxicity. *Journal of Environmental Sciences*, 24(3), pp.479-487.
- Eswaramoorthi, S., Dhanapal, K. and Chauhan, D., 2008. Advances in textile wastewater treatment: the case for UV-Ozonation and membrane bioreactor for common effluent treatment plants in Tirupur, Tamil Nadu, India. *Environmental Technology Awareness Series*.
- Faisal, M., Alsaiani, M., Rashed, M. and Harraz, F., 2021. Highly efficient biomass-derived carbon@Au/ZnO novel ternary photocatalyst for ultra-fast degradation of gemifloxacin drug. *Journal of Materials Research and Technology*, 14, pp.954-967.
- Fagier, M., 2021. Plant-Mediated Biosynthesis and Photocatalysis Activities of Zinc Oxide Nanoparticles: A Prospect towards Dyes Mineralization. *Journal of Nanotechnology*, 2021, pp.1-15.
- Fardood, S., Moradnia, F., Forootan, R., Abbassi, R., Jalalifar, S., Ramazani, A. and Sillanpää, M., 2022. Facile green synthesis, characterization and visible light photocatalytic activity of MgFe₂O₄@CoCr₂O₄ magnetic nanocomposite. *Journal of Photochemistry and Photobiology A: Chemistry*, 423, p.113621.

- Fonseca, T., Relógio, P., Martinho, J. and Farinha, J., 2007. Preparation and Surface Characterization of Polymer Nanoparticles Designed for Incorporation into Hybrid Materials. *Langmuir*, 23(10), pp.5727-5734.
- Fu, Y., Wang, Y., Zhao, H., Zhang, Z., An, B., Bai, C., Ren, Z., Wu, J., Li, Y., Liu, W., Li, P. and Ma, J., 2021. Synthesis of ternary ZnO/ZnS/MoS₂ piezoelectric nanoarrays for enhanced photocatalytic performance by conversion of dual heterojunctions. *Applied Surface Science*, 556, p.149695.
- Gao, C., Low, J., Long, R., Kong, T., Zhu, J. and Xiong, Y., 2020. Heterogeneous Single-Atom Photocatalysts: Fundamentals and Applications. *Chemical Reviews*, 120(21), pp.12175-12216.
- Gao, Y., Fang, X., Chen, D., Ma, N. and Dai, W., 2022. Ternary photocatalyst of ZIF-8 nanofilms coupled with AgI nanoparticles seamlessly on ZnO microrods for enhanced visible-light photocatalysis degradation. *Journal of the Taiwan Institute of Chemical Engineers*, 131, p.104146.
- Garcia-Muñoz, P., Fresno, F., de la Peña O'Shea, V. and Keller, N., 2019. Ferrite Materials for Photoassisted Environmental and Solar Fuels Applications. *Topics in Current Chemistry*, 378(1), pp.2-3.
- Ghaly, A., Ananthashankar, R., Alhattab, M. and Ramakrishnan, V., 2014. Production, Characterization and Treatment of Textile Effluents: A Critical Review. *Journal of Chemical Engineering & Process Technology*, 05(01), pp.1-18.
- Gholami, P., Dinpazhoh, L., Khataee, A. and Orooji, Y., 2019. Sonocatalytic activity of biochar-supported ZnO nanorods in degradation of gemifloxacin: Synergy study, effect of parameters and phytotoxicity evaluation. *Ultrasonics Sonochemistry*, 55, pp.44-56.
- Han, J., Liu, Y., Singhal, N., Wang, L. and Gao, W., 2012. Comparative photocatalytic degradation of estrone in water by ZnO and TiO₂ under artificial UVA and solar irradiation. *Chemical Engineering Journal*, 213, pp.150-162.
- Hanafi, M. and Sapawe, N., 2020. A review on the water problem associate with organic pollutants derived from phenol, methyl orange, and remazol brilliant blue dyes. *Materials Today: Proceedings*, 31, pp.A141-A150.

- Hashmi, S., Shah, M., Muhammad, W., Ahmad, A., Ullah, M., Nadeem, M. and Abbasi, B., 2021. Potentials of phyto-fabricated nanoparticles as ecofriendly agents for photocatalytic degradation of toxic dyes and wastewater treatment, risk assessment and probable mechanism. *Journal of the Indian Chemical Society*, 98(4), p.100019.
- Hassanshahi, N. and Karimi-Jashni, A., 2018. Comparison of photo-Fenton, O₃/H₂O₂/UV and photocatalytic processes for the treatment of gray water. *Ecotoxicology and Environmental Safety*, 161, pp.683-690.
- Heidari, P. and Masoudpanah, S., 2021. Structural, magnetic and optical properties and photocatalytic activity of magnesium-calcium ferrite powders. *Journal of Physics and Chemistry of Solids*, 148, p.109681.
- Ho, J., Ooi, J., Wan, Y. and Andiappan, V., 2021. Synthesis of wastewater treatment process (WWTP) and supplier selection via Fuzzy Analytic Hierarchy Process (FAHP). *Journal of Cleaner Production*, 314, p.128104.
- Ibhadon, A. and Fitzpatrick, P., 2013. Heterogeneous Photocatalysis: Recent Advances and Applications. *Catalysts*, 3(1), pp.189-218.
- Ikram, M., Khan, M., Raza, A., Imran, M., Ul-Hamid, A. and Ali, S., 2020. Outstanding performance of silver-decorated MoS₂ nanopetals used as nanocatalyst for synthetic dye degradation. *Physica E: Low-dimensional Systems and Nanostructures*, 124, p.114246.
- Imran, M., Haider, S., Ahmad, K., Mahmood, A. and Al-masry, W., 2017. Fabrication and characterization of zinc oxide nanofibers for renewable energy applications. *Arabian Journal of Chemistry*, 10, pp.S1067-S1072.
- Israr, M., Iqbal, J., Arshad, A., Gómez-Romero, P. and Benages, R., 2020. Multifunctional MgFe₂O₄/GNPs nanocomposite: Graphene-promoted visible light driven photocatalytic activity and electrochemical performance of MgFe₂O₄ nanoparticles. *Solid State Sciences*, 110, p.106363.
- Janani, B., Syed, A., Thomas, A., Al-Rashed, S., Elgorban, A., Raju, L. and Khan, S., 2021. A simple approach for the synthesis of bi-functional p-n type ZnO@CuFe₂O₄ heterojunction nanocomposite for photocatalytic and antimicrobial application. *Physica E: Low-dimensional Systems and Nanostructures*, 130, p.114664.

- Jiang, Z., Chen, K., Zhang, Y., Wang, Y., Wang, F., Zhang, G. and Dionysiou, D., 2020. Magnetically recoverable MgFe₂O₄/conjugated polyvinyl chloride derivative nanocomposite with higher visible-light photocatalytic activity for treating Cr(VI)-polluted water. *Separation and Purification Technology*, 236, p.116272.
- Johnson, I., Ali, M. and Kumar, M., 2019. Cyanobacteria/Microalgae for Distillery Wastewater Treatment- Past, Present and the Future. *Microbial Wastewater Treatment*, pp.195-236.
- Joshiba, G., Kumar, P., Govarathanan, M., Ngueagni, P., Abilarasu, A. and Carolin C, F., 2021. Investigation of magnetic silica nanocomposite immobilized *Pseudomonas fluorescens* as a biosorbent for the effective sequestration of Rhodamine B from aqueous systems. *Environmental Pollution*, 269, p.116173.
- Jyothi, N. and Ravichandran, K., 2020. Optimum pH for effective dye degradation: Mo, Mn, Co and Cu doped ZnO photocatalysts in thin film form. *Ceramics International*, 46(14), pp.23289-23292.
- Kandhasamy, D., Selvaraju, C. and Dharuman, V., 2021. Structure and dynamics of poly(methacrylic acid) and its interpolymer complex probed by covalently bound rhodamine-123. *Spectrochimica Acta Part A: Molecular and Biomolecular Spectroscopy*, 248, p.119166.
- Kang, X., Liu, S., Dai, Z., He, Y., Song, X. and Tan, Z., 2019. Titanium Dioxide: From Engineering to Applications. *Catalysts*, 9(2), p.191.
- Kansal, S., Singh, M. and Sud, D., 2007. Studies on photodegradation of two commercial dyes in aqueous phase using different photocatalysts. *Journal of Hazardous Materials*, 141(3), pp.581-590.
- Keskin, B., Ersahin, M., Ozgun, H. and Koyuncu, I., 2021. Pilot and full-scale applications of membrane processes for textile wastewater treatment: A critical review. *Journal of Water Process Engineering*, 42, p.102172.
- Kallerhoff, J., Arshad, M. and Bilal, M., 2021. Graphene quantum dot and iron co-doped TiO₂ photocatalysts: Synthesis, performance evaluation and phytotoxicity studies. *Ecotoxicology and Environmental Safety*, 226, p.112855.
- Khalil, M. and Liu, Y., 2021. Greywater biodegradability and biological treatment technologies: A critical review. *International Biodeterioration & Biodegradation*, 161, p.105211.

- Khan, M., Riaz, N., Shaikh, A., Shah, J., Hussain, J., Irshad, M., Awan, M., Syed, A., Khataee, A. and Fathinia, M., 2013. Recent Advances in Photocatalytic Processes by Nanomaterials. *New and Future Developments in Catalysis*, pp.267-288.
- Kilic, Z., 2020. The importance of water and conscious use of water. *International Journal of Hydrology*, 4(5), pp.239-241.
- Kim, S. and Park, C., 2021. Potential of ceramic ultrafiltration membranes for the treatment of anionic surfactants in laundry wastewater for greywater reuse. *Journal of Water Process Engineering*, 44, p.102373.
- Kumar, G., Cho, H., Lee, D., Kumar, J., Siva, C., Ilanchezhian, P., Kim, D. and Kang, T., 2021. Elevating the charge separation of MgFe₂O₄ nanostructures by Zn ions for enhanced photocatalytic and photoelectrochemical water splitting. *Chemosphere*, 283, p.131134.
- Kumari, M., Devi, L., Maia, G., Chen, T., Al-Zaqri, N. and Ali, M., 2022. Mechanochemical synthesis of ternary heterojunctions TiO₂(A)/TiO₂(R)/ZnO and TiO₂(A)/TiO₂(R)/SnO₂ for effective charge separation in semiconductor photocatalysis: A comparative study. *Environmental Research*, 203, p.111841.
- Le, T., Nguyen, T., Hoang, C., Nguyen, D., Lund, T., Nguyen, H. and Huynh, T., 2020. Formation of surface defects by thermal shock method for the improved photocatalytic activity of ZnO nanoparticles. *Journal of Asian Ceramic Societies*, 8(1), pp.193-202.
- Lee, Y., Fujimoto, T., Yamanaka, S. and Kuga, Y., 2021. Evaluation of photocatalysis of Au supported ZnO prepared by the spray pyrolysis method. *Advanced Powder Technology*,.
- Li, S., Ma, Z., Zhang, J., Wu, Y. and Gong, Y., 2008. A comparative study of photocatalytic degradation of phenol of TiO₂ and ZnO in the presence of manganese dioxides. *Catalysis Today*, 139(1-2), pp.109-112.
- Liu, H., Wang, C. and Wang, G., 2020. Photocatalytic Advanced Oxidation Processes for Water Treatment: Recent Advances and Perspective. *Chemistry – An Asian Journal*, 15(20), pp.3239-3253.
- Liu, R., Tan, C., Li, J. and Zuo, J., 2021. Rational design of a novel C/ZnO/BiOI composite for efficient visible-light-driven photocatalysis. *Materials Letters*, p.130564.

- Liu, Y., Zhang, Q., Yuan, H., Luo, K., Li, J., Hu, W., Pan, Z., Xu, M., Xu, S., Levchenko, I. and Bazaka, K., 2021. Comparative study of photocatalysis and gas sensing of ZnO/Ag nanocomposites synthesized by one- and two-step polymer-network gel processes. *Journal of Alloys and Compounds*, 868, p.158723.
- Lyu, J., Hu, Z., Li, Z. and Ge, M., 2019. Removal of tetracycline by BiOBr microspheres with oxygen vacancies: Combination of adsorption and photocatalysis. *Journal of Physics and Chemistry of Solids*, 129, pp.61-70.
- Mahendran, V. and Gogate, P., 2021. Degradation of Acid Scarlet 3R dye using oxidation strategies involving photocatalysis based on Fe doped TiO₂ photocatalyst, ultrasound and hydrogen peroxide. *Separation and Purification Technology*, 274, p.119011.
- MIDA, 2016. *2016 MALAYSIA: Investment Performance Report*. [online] Mida.gov.my. Available at: <https://mida.gov.my/wp-content/uploads/2020/12/20171101140914_MIDA-FINAL20MIPR2016.pdf> [Accessed 5 August 2021].
- Moiz, M., Mumtaz, A., Salman, M., Wilayat Husain, S., Baluch, A. and Ramzan, M., 2021. Band Gap Engineering of ZnO via Transition Metal Doping: An ab initio Study. *Chemical Physics Letters*, p.138979.
- Moradi, M., Hasanvandian, F., Isari, A., Hayati, F., Kakavandi, B. and Setayesh, S., 2021. CuO and ZnO co-anchored on g-C₃N₄ nanosheets as an affordable double Z-scheme nanocomposite for photocatalytic decontamination of amoxicillin. *Applied Catalysis B: Environmental*, 285, p.119838.
- Morkoç, H. and Özgür, U., 2009. *Zinc oxide*. Weinheim: Wiley-VCH, pp.1-76.
- Nandi, P. and Das, D., 2021. ZnO/CdS/CuS heterostructure: A suitable candidate for applications in visible-light photocatalysis. *Journal of Physics and Chemistry of Solids*, 160, p.110344.
- Naraginti, S. and Yong, Y., 2019. Enhanced detoxification of p-bromophenol by novel Zr/Ag-TiO₂@rGO ternary composite: Degradation kinetics and phytotoxicity evolution studies. *Ecotoxicology and Environmental Safety*, 170, pp.355-362.

- Nguyen, C., Tran, M., Tran, T. and Juang, R., 2020. Enhanced removal of various dyes from aqueous solutions by UV and simulated solar photocatalysis over TiO₂/ZnO/rGO composites. *Separation and Purification Technology*, 232, p.115962.
- Noman, E., Al-Gheethi, A., Talip, B., Mohamed, R. and Kassim, A., 2020. Decolourization of Dye Wastewater by A Malaysian isolate of *Aspergillus iizukae* 605EAN Strain: A Biokinetic, Mechanism and Microstructure Study. *International Journal of Environmental Analytical Chemistry*, 101(11), pp.1592-1615.
- Nonakaran, B. and Yangjeh, A., 2016. Ternary ZnO/AgI/Ag₂CO₃ nanocomposites: Novel visible-light-driven photocatalysts with excellent activity in degradation of different water pollutants. *Materials Chemistry and Physics*, 184, pp.210-221.
- Oh, K., Leong, J., Poh, P., Chong, M. and Lau, E., 2018. A review of greywater recycling related issues: Challenges and future prospects in Malaysia. *Journal of Cleaner Production*, 171, pp.17-29.
- Ojha, D., Karki, H. and Kim, H., 2018. Design of ternary hybrid ATO/g-C₃N₄/TiO₂ nanocomposite for visible-light-driven photocatalysis. *Journal of Industrial and Engineering Chemistry*, 61, pp.87-96.
- Ong, C., Ng, L. and Mohammad, A., 2018. A review of ZnO nanoparticles as solar photocatalysts: Synthesis, mechanisms and applications. *Renewable and Sustainable Energy Reviews*, 81, pp.536-551.
- Ong, Z., Asadsangabifard, M., Ismail, Z., Tam, J. and Roushenas, P., 2019. Design of a compact and effective greywater treatment system in Malaysia. *DESALINATION AND WATER TREATMENT*, 146, pp.141-151.
- Oteng-Pepurah, M., Acheampong, M. and deVries, N., 2018. Greywater Characteristics, Treatment Systems, Reuse Strategies and User Perception—a Review. *Water, Air, & Soil Pollution*, 229(8).
- Pang, Y. and Abdullah, A., 2013. Current Status of Textile Industry Wastewater Management and Research Progress in Malaysia: A Review. *CLEAN - Soil, Air, Water*, 41(8), pp.751-764.

- Pathak, H., Patel, S., Rathod, M. and Chauhan, K., 2011. In vitro studies on degradation of synthetic dye mixture by *Comamonas* sp. VS-MH2 and evaluation of its efficacy using simulated microcosm. *Bioresource Technology*, 102(22), pp.10391-10400.
- Pirhashemi, M. and Yangjeh, A., 2015. Ternary ZnO/AgBr/Ag₂CrO₄ nanocomposites with tandem n–n heterojunctions as novel visible-light-driven photocatalysts with excellent activity. *Ceramics International*, 41(10), pp.14383-14393.
- Popkin, B., D'Anci, K. and Rosenberg, I., 2010. Water, hydration, and health. *Nutrition Reviews*, 68(8), pp.439-458.
- Priyanka, K., Remya, N. and Behera, M., 2020. Greywater treatment using modified solar photocatalyst- degradation, kinetics, pathway and toxicity analysis. *Separation and Purification Technology*, 251, p.117319.
- Qamar, M., Javed, M., Shahid, S., Iqbal, S., Abubshait, S., Abubshait, H., Ramay, S., Mahmood, A. and Ghaithan, H., 2021. Designing of highly active g-C₃N₄/Co@ZnO ternary nanocomposites for the disinfection of pathogens and degradation of the organic pollutants from wastewater under visible light. *Journal of Environmental Chemical Engineering*, 9(4), p.105534.
- Qin, M., Jin, K., Li, X., Wang, R., Li, Y. and Wang, H., 2022. Novel highly-active Ag/Bi dual nanoparticles-decorated BiOBr photocatalyst for efficient degradation of ibuprofen. *Environmental Research*, 206, p.112628.
- Qian, R., Zong, H., Schneider, J., Zhou, G., Zhao, T., Li, Y., Yang, J., Bahnemann, D. and Pan, J., 2019. Charge carrier trapping, recombination and transfer during TiO₂ photocatalysis: An overview. *Catalysis Today*, 335, pp.78-90
- Rafiq, A., Ikram, M., Ali, S., Niaz, F., Khan, M., Khan, Q. and Maqbool, M., 2021. Photocatalytic degradation of dyes using semiconductor photocatalysts to clean industrial water pollution. *Journal of Industrial and Engineering Chemistry*, 97, pp.111-128.
- Rasiah, R., 2009. Malaysia's Textile and Garment Firms at the Crossroads. *Journal of Contemporary Asia*, 39(4), pp.530-542.
- Sa-nguanprang, S., Phuruangrat, A., Thongtem, T. and Thongtem, S., 2020. Characterization and photocatalysis of visible-light-driven Dy-doped ZnO nanoparticles synthesized by

tartaric acid-assisted combustion method. *Inorganic Chemistry Communications*, 117, p.107944.

Saha, S., 2012. *Molecular Photochemistry - Various Aspects*. p.204.

Shreya, Verma, A., Dash, A., Bhunia, P. and Dash, R., 2021. Removal of surfactants in greywater using low-cost natural adsorbents: A review. *Surfaces and Interfaces*, 27, p.101532.

Sin, J., Lim, C., Lam, S., Mohamed, A. and Zeng, H., 2019. Facile synthesis of novel ZnO/Nd-doped BiOBr composites with boosted visible light photocatalytic degradation of phenol. *Materials Letters*, 248, pp.20-23.

Song, M., Qi, K., Wen, Y., Zhang, X., Yuan, Y., Xie, X. and Wang, Z., 2021. Rational design of novel three-dimensional reticulated Ag₂O/ZnO Z-scheme heterojunction on Ni foam for promising practical photocatalysis. *Science of The Total Environment*, 793, p.148519.

Syed, A., Elgorban, A., Bahkali, A. and Zaghloul, N., 2021. Coupling of nano-spinel MgFe₂O₄ on Co₃O₄ for heterogeneous photocatalysis and antibacterial applications: Insights of optoelectrical properties. *Colloid and Interface Science Communications*, 44, p.100467.

Tan, H., Abdi, F. and Ng, Y., 2019. Heterogeneous photocatalysts: an overview of classic and modern approaches for optical, electronic, and charge dynamics evaluation. *Chemical Society Reviews*, 48(5), pp.1255-1271.

Thomson, C., Lee, A. and Vilela, F., 2020. Heterogeneous photocatalysis in flow chemical reactors. *Beilstein Journal of Organic Chemistry*, 16, pp.1495-1549.

Tian, C., Zhang, Q., Wu, A., Jiang, M., Liang, Z., Jiang, B. and Fu, H., 2012. Cost-effective large-scale synthesis of ZnO photocatalyst with excellent performance for dye photodegradation. *Chemical Communications*, 48(23), p.2858.

Topare, N., Bhutada, D. and Bansod, P., 2021. Application of TiO₂ and Nb₂O₅ for ultrasonic degradation of Rhodamine-B. *Materials Today: Proceedings*.

Tu, X., Ke, S., Luo, S., Zhou, R., Zeng, Z. and Luo, S., 2021. Self-supporting rGO/BiOBr composite on loofah-sponge as a floating monolithic photocatalyst for efficient microcystis aeruginosa inactivation. *Separation and Purification Technology*, 275, p.119226.

- Turhan, K. and Turgut, Z., 2009. Decolorization of direct dye in textile wastewater by ozonization in a semi-batch bubble column reactor. *Desalination*, 242(1-3), pp.256-263.
- Vaiano, V., Jaramillo-Paez, C., Matarangolo, M., Navío, J. and del Carmen Hidalgo, M., 2019. UV and visible-light driven photocatalytic removal of caffeine using ZnO modified with different noble metals (Pt, Ag and Au). *Materials Research Bulletin*, 112, pp.251-260.
- Vaiano, V., Sannino, D. and Sacco, O., 2020. Heterogeneous photocatalysis. *Nanomaterials for the Detection and Removal of Wastewater Pollutants*, pp.285-301.
- Venkatesh, N. and Sakthivel, P., 2022. Efficient degradation of azo dye pollutants on Zn doped SnO₂ photocatalyst under sunlight irradiation: Performance, mechanism and toxicity evaluation. *Inorganic Chemistry Communications*, 139, p.109360.
- Vijay, N., Wu, S. and Velmathi, S., 2019. Turn on fluorescent chemosensor containing rhodamine B fluorophore for selective sensing and in vivo fluorescent imaging of Fe³⁺ ions in HeLa cell line and zebrafish. *Journal of Photochemistry and Photobiology A: Chemistry*, 384, p.112060.
- Waheed, I., Yasin Thayee Al-Janabi, O. and Foot, P., 2022. Novel MgFe₂O₄-CuO/GO heterojunction magnetic nanocomposite: Synthesis, characterization, and batch photocatalytic degradation of methylene blue dye. *Journal of Molecular Liquids*, 357, p.119084.
- Wang, J., Zhang, Q., Deng, F., Luo, X. and Dionysiou, D., 2020. Rapid toxicity elimination of organic pollutants by the photocatalysis of environment-friendly and magnetically recoverable step-scheme SnFe₂O₄/ZnFe₂O₄ nano-heterojunctions. *Chemical Engineering Journal*, 379, p.122264.
- Wang, M., Tan, G., Ren, H., Xia, A. and Liu, Y., 2019. Direct double Z-scheme O-g-C₃N₄/Zn₂SnO₄N/ZnO ternary heterojunction photocatalyst with enhanced visible photocatalytic activity. *Applied Surface Science*, 492, pp.690-702.
- Wang, X., Xu, G., Tu, Y., Wu, D., Li, A. and Xie, X., 2021. BiOBr/PBCD-B-D dual-function catalyst with oxygen vacancies for Acid Orange 7 removal: Evaluation of adsorption-photocatalysis performance and synergy mechanism. *Chemical Engineering Journal*, 411, p.128456.

- Wei, X., Yang, X., Xu, X., Liu, Z., Naraginti, S. and Wan, J., 2021. Novel magnetically separable tetrahedral $\text{Ag}_3\text{PO}_4/\text{NrGO}/\text{CuFe}_2\text{O}_4$ photocatalyst for efficient detoxification of 2,4-dichlorophenol. *Environmental Research*, 201, p.111519.
- Wong, S., Yac'cob, N., Ngadi, N., Hassan, O. and Inuwa, I., 2018. From pollutant to solution of wastewater pollution: Synthesis of activated carbon from textile sludge for dye adsorption. *Chinese Journal of Chemical Engineering*, 26(4), pp.870-878.
- Xu, L., Cui, Q., Tian, Y., Jiao, A., Zhang, M., Li, S., Li, H. and Chen, M., 2021. Enhanced synergistic coupling effect of ternary $\text{Au}/\text{Ag}/\text{AgCl}$ nanochains for promoting natural-solar-driven photocatalysis. *Applied Surface Science*, 545, p.149054.
- Xu, D. and Ma, H., 2021. Degradation of rhodamine B in water by ultrasound-assisted TiO_2 photocatalysis. *Journal of Cleaner Production*, 313, p.127758.
- Xue, Y., Chang, Q., Hu, X., Cai, J. and Yang, H., 2020. A simple strategy for selective photocatalysis degradation of organic dyes through selective adsorption enrichment by using a complex film of CdS and carboxymethyl starch. *Journal of Environmental Management*, 274, p.111184.
- Yamashita, H., Tanaka, A., Nishimura, M., Koyano, K., Tatsumi, T. and Anpo, M., 1998. Photochemical properties of Rhodamine-B dye molecules included within mesoporous molecular sieves. *Studies in Surface Science and Catalysis*, pp.551-558.
- Yaseen, D. and Scholz, M., 2018. Textile dye wastewater characteristics and constituents of synthetic effluents: a critical review. *International Journal of Environmental Science and Technology*, 16(2), pp.1193-1226.
- Yashni, G., Al-Gheethi, A., Radin Mohamed, R., Dai-Viet, N., Al-Kahtani, A., Al-Sahari, M., Nor Hazhar, N., Noman, E. and Alkhadher, S., 2021. Bio-inspired ZnO NPs synthesized from *Citrus sinensis* peels extract for Congo red removal from textile wastewater via photocatalysis: Optimization, mechanisms, techno-economic analysis. *Chemosphere*, 281, p.130661.
- Yuan, X., Wang, H., Wu, Y., Chen, X., Zeng, G., Leng, L. and Zhang, C., 2015. A novel SnS_2 - MgFe_2O_4 /reduced graphene oxide flower-like photocatalyst: Solvothermal synthesis, characterization and improved visible-light photocatalytic activity. *Catalysis Communication*, 61, pp.62-66.

- Zarezadeh, S., Habibi-Yangjeh, A., Mousavi, M. and Ghosh, S., 2020. Synthesis of novel p-n-p BiOBr/ZnO/BiOI heterostructures and their efficient photocatalytic performances in removals of dye pollutants under visible light. *Journal of Photochemistry and Photobiology A: Chemistry*, 389, p.112247.
- Zhang, D. and Zeng, F., 2017. Significantly enhanced photocatalytic performance of zinc oxide via bismuth oxybromide hybridization and the mechanism study. *Journal of the Iranian Chemical Society*, 14(10), pp.2055-2066.
- Zhang, Y., Zhang, H., Chang, F., Xie, P., Liu, Q., Duan, L., Wu, H., Zhang, X., Peng, W., Liu, F. and Xu, L., 2021. In-situ responses of phytoplankton to graphene photocatalysis in the eutrophic lake Xingyun, southwestern China. *Chemosphere*, 278, p.130489.
- Zhong, N., Yuan, J., Luo, Y., Zhao, M., Luo, B., Liao, Q., Chang, H., Zhong, D. and Rittmann, B., 2021. Intimately coupling photocatalysis with phenolics biodegradation and photosynthesis. *Chemical Engineering Journal*, 425, p.130666.
- Zhu, P., Ren, Z., Wang, R., Duan, M., Xie, L., Xu, J. and Tian, Y., 2019. Preparation and visible photocatalytic dye degradation of Mn-TiO₂/sepiolite photocatalysts. *Frontiers of Materials Science*, 14(1), pp.33-42.
- Zubair, M., Aziz, H., Ahmad, M., Ihsanullah, I. and Al-Harhi, M., 2021. Adsorption and reusability performance of M-Fe (M = Co, Cu, Zn and Ni) layered double hydroxides for the removal of hazardous Eriochrome Black T dye from different water streams. *Journal of Water Process Engineering*, 42, p.102060.